February 2022
Doctoral Degree Dissertation

Path Loss Characterization of Outdoor and Indoor Microwave Links

Graduate School of Chosun University

Department of Information and Communication Engineering

Md Abdus Samad

Path Loss Characterization of Outdoor and Indoor Microwave Links

실외 및 실내에서 마이크로파 링크의 경로손실 특성

February 25, 2022

Graduate School of Chosun University

Department of Information and Communication Engineering

Md Abdus Samad

Path Loss Characterization of Outdoor and Indoor Microwave Links

Advisor: Prof. Dong-You Choi, PhD

This thesis is submitted to the Graduate School of Chosun University in partial fulfillment of the requirements for the Doctor's degree engineering.

October, 2021

Graduate School of Chosun University

Department of Information and Communication Engineering

Md Abdus Samad

This is to certify that the Doctoral degree dissertation of

Md Abdus Samad

has been approved by examining committee for the thesis requirement for the Doctoral degree in Engineering.

Committee Chairperson	Prof. Goo-Rak Kwon	(Sign)
Committee Member	Prof. Bum-Shik Lee	(Sign)
Committee Member	Prof. Sun-Kuk Noh	(Sign)
Committee Member	Prof. Tae-Soon Yun	(Sign)
Committee Member	Prof. Dong-You Choi	(Sign)

January 2022

Graduate School of Chosun University

Abstract

Path Loss Characterization of Outdoor and Indoor Microwave Links.

Author: Md Abdus Samad
Advisor: Prof. Dong-You Choi, PhD
Depart. of Info. and Comm. Engg.
Graduate School of Chosun University

Several disturbances limit the quality of radio links at higher frequency bands in outdoor and indoor usage. In outdoor use, among other atmospheric factors, rainfall is the significant propagation impairment at millimetric wavebands, which needs to be considered during the link budget planning. Moreover, for indoor usage, the blockage material exists along with the transmitted wave that results in scattering, reflection, diffraction, dispersion, and penetration problems that create path loss of the propagated wave. Consequently, it is essential to know the path loss both for the outdoor and indoor microwave links. Because knowing the expected attenuation, it is possible to set the power level at the transmitter side (within the permissible level). This investigation discusses the path loss characteristics in both outdoor and indoor links and proposes new methods of path loss prediction in outdoor and indoor links. Three years of rainfall and received signal power were measured over four terrestrial links to estimate rain attenuation. And using the measured received signal power — three existing attenuation models, ITU-R 530.17, Lin, and revised Silva Mello models, were compared with the measured rain attenuation. It was found that these mod-

els did not correspond with the measured results. Therefore, a supervised learning-based attenuation prediction method was proposed, which provides better performance than existing models. Furthermore, the proposed model with measured received signal level and rainfall data at the above-mentioned operating frequencies was validated. Another experiment measured the received power of earth-space links data, which were recorded from 2013 to 2015 through Koreasat 6 satellite at 12.25 and 20.73 GHz. In that experiment, the previously mentioned terrestrial link data and the earth-space links data were validated with the existing ITU-R long-term frequency, and it was found that the current ITU-R long-term frequency scaling technique did not perform well in South Korea. Consequently, a new scaling technique was proposed using artificial neural networks. The experimental results confirm that the proposed artificial neural network (ANN)-based scaling model showed superior performance in predicting attenuation for frequency scaling for outdoor terrestrial and slant links. The existing path loss model for indoor corridor links usually uses the attenuation resulting from individual elements path loss of the propagated wave — which is challenging to compute. And in the case of path loss modeling inside the tunnel, modal expansion, numeric methods Finite Difference Time Domain (FDTD), Crank Nicolson (CN), Vector Parabolic Equation (VPE), Scalar Parabolic Equation (SPE), Uniform Theory of Diffraction (UTD), Ray-Tracing Technique (RT), Tapped Delay Line (TDL) is used. All of these methods are too complex considering the computing procedure. On the other hand, a large-scale path loss technique can predict attenuation in a gross sense without computing individual element effects in the indoor corridors and tunnels — which

is computationally efficient. Therefore, large-scale path losses of LOS links in the extended indoor corridor and 1.7 km long train tunnel environments were simulated using real observed path loss datasets at 3.7 and 28 GHz. The minimum mean square error (MMSE) approach was used to evaluate the distance and frequency-dependent optimized coefficients of the large-scale models: close-in (CI) model with a frequency-weighted path loss exponent (CIF), floating-intercept (FI), and alpha-beta–gamma (ABG) models. The outcome of the indoor corridor showed that the large-scale FI and CI models fitted the measured results at 3.7 and 28 GHz. The tunnel data outcome showed a comparatively lower ($n<2$) path loss exponent inside the tunnel compared to the outdoor environment. In the tunnel, the FI model outperformed all examined models as it yielded a path loss closer to the measured datasets and a minimum standard deviation of the shadow factor.

국 문 요 약

실외 및 실내에서 마이크로파 링크의 경로손실 특성.

저자: 엠디 압두스 사마드
지도교수: 최동유
조선대학교 대학원 정보통신공학과

실내 및 실외에서 무선 링크의 품질은 사용주파수가 높아질수록 많은 영향을 받는다. 실외의 경우 많은 대기 요인 중 강우강도는 밀리미터파 대역에서 전파경로 손실에 많은 영향을 주고 있으며, 링크버짓 (link budget)을 위해 충분히 고려해야 한다. 실내의 경우 장애물로 인한 산란, 반사, 회절, 분산 및 침투 등이 전파 경로손실의 주요 요인이다. 결과적으로, 전파 경로손실을 예측함으로써 송신 측에서 전력 레벨을 설정하기 위하여 실내 및 실외 전파 경로손실에 대해 아는 것이 중요하다.

따라서 본 논문에서는 실내 및 실외 전파환경에서 경로손실에 대해 연구하였다. 실외 밀리미터파 대역에서의 강우감쇠를 추정하기 위해 강우강도와 수신신호 전력은 4개의 지상 링크를 대상으로 3년간 측정한 데이터를 사용하였으며, 기존에 강우감쇠 예측을 위해 널리 활용되고 있는 ITU-R 530.17, Lin 모델, Revised Silva Mello 모델의 예측값과 비교하였다. 실측값과 예측값의 비교 결과, 차이가 남에 따라 기존 모델보다 더 나은 예측값을 제공하기 위하여 지도 학습 기반 강우감쇠 예측 방법을 제안하였고, 제안된 모델의 예측값과 강우감쇠 실측값을 비교 및 분석 함으로써 제안 모델의 적정성을 확인하였다.

또한, 다른 주파수 대역과 편파에 대한 스케일링 (scaling) 기법을 연구하기 위하여 2013년부터 2015년까지 무궁화위성 6호의 12.25 GHz와 20.73 GHz

대역의 데이터를 사용하였으며, ANN (Artificial Neural Network) 기반의 새로운 스케일링 기법을 제안하였다. 비교 및 분석 결과, 제안한 스케일링 예측 모델이 만족함을 확인하였다.

일반적으로 건물 내 복도 링크에 대한 기존 경로손실 예측 모델은 전파전파(wave propagation)의 개별적 경로손실 감쇠 요소를 활용하지만 계산하기가 복잡하다. 그리고 열차 터널 내부 경로손실 모델링의 경우, FDTD (Finite Difference Time Domain), CN (Crank Nicolson), VPE (Vector Parabolic Equation), SPE (Scalar Parabolic Equation), UTD (Uniform Theory of Diffraction), RT (Ray-tracing Technique), TDL (Tapped Delay Line)를 활용하고 있으며, 이러한 모든 방법은 계산 절차를 고려할 때 너무 복잡하다. 반면에 large-scale 경로손실 예측 기법은 건물 내 복도와 열차 터널 환경하에서 개별적 경로손실 감쇠 요소 효과를 계산하지 않고도 총체적인 의미에서 감쇠를 예측할 수 있기 때문에 효율적으로 계산할 수 있다.

본 논문에서는 건물 내 복도와 1.7 km 길이의 열차 터널 환경하에서의 전파전파 특성을 분석하기 위해 5G 주파수 대역인 3.7 GHz와 28 GHz에 대해 혼 안테나와 TAS (Tracking Antenna System)를 사용하여 측정하였으며, 실측 데이터는 FI, CI, CIF 및 ABG 모델과 같은 전파전파 예측 모델의 예측값과 비교 및 분석하였다. 터널 환경하에서의 비교 및 분석 결과, 비교적 낮은 전파경로 손실 지수 ($n < 2$)를 나타내었다. 특히, FI 모델의 예측값이 실측값과 유사함을 확인하였다.

Acknowledgements

In the name of Allah, the Most Gracious, the Most Merciful. First of all, I would like to thank Allah, the Almighty, for all the copious blessings of my life.

I want to express my profound and sincere gratitude to my advisor, Prof. Dong-You Choi. His invaluable support, encouragement, supervision, and valuable suggestions throughout the doctoral research have provided a strong base for completing my thesis. It is an honor to work under his direction with insightful advice. Besides, I wish to express my warm and sincere thanks to the thesis committee members – Prof. Goo-Rak Kwon, Prof. Bum-Shik Lee, Prof. Sun-Kuk Noh, and Prof. Tae-Soon Yun for their constructive comments and invigorating suggestions. Their opinions regarding my research work have helped me enhance and polish this dissertation. I appreciate the efforts of the professors to lay the groundwork for my research projects through classroom teaching. Hence, I respect their time and intriguing suggestions for improving the effectiveness and engagement of my learning experience.

I greatly acknowledge the support that I received from Korean Government through Korean Government Scholarship (GKS) program for my doctoral studies. Many thanks to the International Team and Korean Language teachers at Busan University of Foreign Studies – where I learned the Korean language before joining Chosun University (CU) as part of the GKS program. I am incredibly grateful to the International Team of CU for their helpful directions and unconditional support throughout this study. Thanks to Sun-Woong Kim, Hyeongjung Kim, In-Kyu Kim, and Jiwan Ghimire for their kind help and tolerating any odds I caused during my research at the communication and wave propagation lab.

I never find words to express my most profound gratitude to my family. I am so grateful to my parents, brothers, and sisters-in-law for their guidance, unparalleled support, and continuous encouragement, which I will never forget in my life. I greatly acknowledge that completing my dissertation would not have been possible without the support and nurturing of my wife. I am

grateful to my daughters and regret that I could not give them sufficient time to care for them while pursuing my doctoral research.

Finally, thanks should also go to Y. Arafat, A. Haque, H. Haque, A. Nazib, I. Fahim, and S. Rezwan because I received their cooperation during my doctoral study. Mainly, I am deeply indebted to Y. Arafat, S. Hossain, and J. Uddin for providing encouragement and support in my difficult times. Special thanks to the community of Bangladeshi students at CU. I would also like to remember all of my teachers, colleagues, and friends for their outstanding contribution to my life.

January 14, 2022, Gwangju Md Abdus Samad

Contents

List of Tables

List of Figures

Abbreviations

3-D	3-Dimensional
3GPP	3rd Generation Partnership Project
ABG	Alpha-Beta-Gamma
ANN	Artificial Neural Network
BER	Bit Error Rate
BW	Bandwidth
CCDF	Complementary Cumulative Distribution Function
CDF	Cumulative Distribution Function
CI	Close-In
CIF	CI model with a Frequency-weighted path loss exponent
CN	Crank Nicolson
COST	European Cooperation in Science and Technology
CU	Chosun University
CW	Continuous sinusoidal Wave
DL	Delay Line
eMBB	Enhanced Mobile Broadband
EMI	Electromagnetic Interference
FDTD	Finite Difference Time Domain
FI	Floating-Intercept
FSPL	Free Space Path Loss
GPS	Global Positioning System
H-H	Horizontal-Horizontal polarization
HP	Horizontal Polarization

IF	Intermediate Frequency
ITU-R	International Telecommunication Union- Radio-communication sector
KT	Korea Telecom
LNA	Low Noise Amplifier
LOS	Line-of-Sight
METIS	Mobile and wireless communications Enablers for Twenty-Twenty Information Society
MMSE	Minimum Mean Square Error
mmWave	Millimeter-Wave
MSE	Mean Squared Error
N/LOS	Non-Line-of-Sight and Line-of-Sight
NLOS	Non-Line-of-Sight
NYU	New York University
P2P	Point-to-Point
PDF	Probability Density Function
PEC	Perfect Electrical Conductor
PLE	Path Loss Exponent
RRA	National Radio Research Agency
RSL	Received Signal Level
RSLs	Received Signal Levels
RSM	Revised Silva Mello
RT	Ray-Tracing Technique
Rx	Receiver
SANN	Supervised Artificial Neural Network

SBRT	Shooting Bouncing Ray Tracing
SF	Shadowing Factor
SPE	Scalar Parabolic Equation
SSB	Single-Sideband (modulation)
STD	Standard Deviation
TAS	Tracking Antenna System
TDL	Tapped Delay Line
Tx	Transmitter
UTD	Uniform Theory of Diffraction
VP	Vertical Polarization
VPE	Vector Parabolic Equation
WINNER	Wireless World Initiative New Radio

1. Introduction

The millimeter-wave frequency spectrum is a good possibility for 5G and future wireless networks. However, it is susceptible to attenuation from indoor and outdoor uses. Because rain is one of the significant factors among other atmospheric elements such as fog, cloud, and gas that create attenuation on the propagation of electromagnetic waves in terrestrial and slant links, on the other hand, the Millimeter-Wave (mmWave) frequency band suffers from high building penetration loss, and more significant delay spread in outdoor to indoor coverage networks, as reported in [1–4]. Presently, 5G primary service locations with high-frequency bands are anticipated to be environments such as internal hotspots and microcells [5]. Consequently, a separate indoor transmission system can promise to ensure better spectral efficiency (and better eMBB services) for indoor network demands. However, only deploying different transmitters inside the indoor will not be helpful if proper transmission of the electromagnetic wave is not modeled according to its internal infrastructure settings and the used materials [6]. Therefore, it needs to find a proper propagation model matching its structure, which can help achieve high-speed data transfer service as per the demands for indoor users.

Figs. 1.1 and 1.2 show the typical common problem of path loss of microwave links, respectively, for the indoor and outdoor wave propagation links.

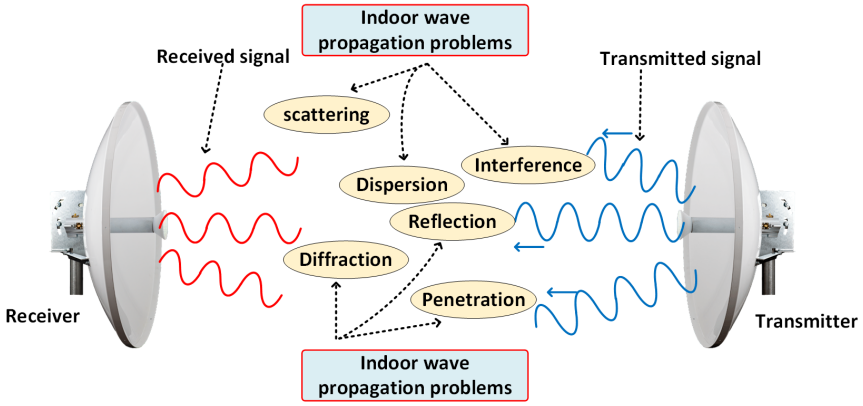

Figure 1.1: Indoor microwave link affected by path loss problems.

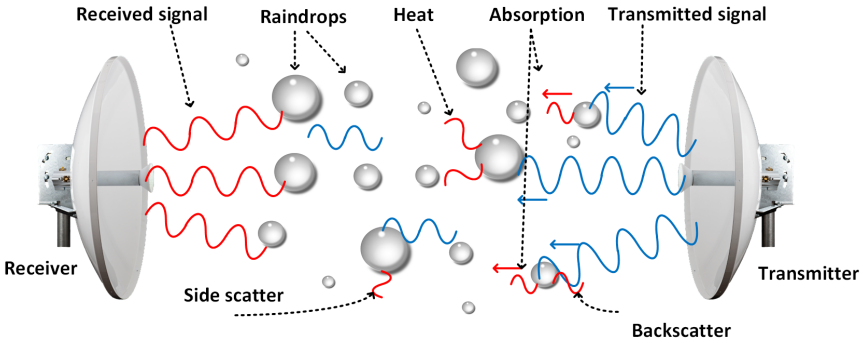

Figure 1.2: Outdoor microwave link affected by rain that results in path loss.

1.1 Propagation Impairment: Outdoor Links

A recent analysis has shown that approximately 50 billion devices will need an Internet connection by 2020; most devices will be wirelessly connected [7]. Rapidly emerging wireless networking systems are beginning to use millimeter-wave to transmit data at a growing pace due to the demands of mobile data network service providers. The rain has a substantial effect on electromagnetic wave propagation. This effect influenced researchers to

control the transmitted power to the counteraction of rain influence on the radio waves. The rain attenuation research is used to study and predict attenuation over a wide variety of frequency bands, especially for bands above 10 GHz [8], in various geographical areas and to identify a suitable model that can estimate attenuation. Identifying the features of a rain attenuation model is one of the most critical activities for creating a model. Several variables can affect rain attenuation, such as the transmitter's distance from the receiver, frequency, rainfall intensity, precipitation, temperature, humidity, density, wind speed, and wind direction. However, rain rate and path length are the essential parameters. As a result, most rain attenuation models evaluate the relationship between rain rate and path length parameters to rain attenuation. To plan the channel capacity, manage the link quality, and network design, reliable rain attenuation in a specific radio link is necessary. Often, if other structures of a communication system operate properly, accessing the possibility of terrestrial or inclined links can be improved with an efficient rain attenuation model. It is also possible to avoid overestimating the transmission system's necessary power by estimating the rain attenuation model. Besides, it is essential to meet the spectrum management regulatory organization specification in each frequency range to comply with the permissible requirements for power transmission. If these requirements are not met, the transmitted signal power can interfere with another neighboring frequency band. This intrusion can cause disruptions to neighboring telecommunications equipment.

Consequently, proper path loss estimation is required due to rain. In this Thesis, to address this path loss problem due to rain, Artificial Neu-

ral Network (ANN)-based models were proposed based on the three years experimentally measured datasets in South Korea.

1.2 Propagation Impairment: Indoor Links

The propagation modeling attempts to anticipate how signals from the transmitter towards the recipient are going. While transmission along with distance, the signal becomes weak, other signal problems such as multi-path fading also arise. The optimal propagation models for particular research rely on the type of communication system, the location it is utilized, and any specific regulatory regulations. Empirical models that use measured data to create a path loss equation model and physical models that employ physical radiowave concepts such as; free-space transmission, reflection, scattering, or diffraction are the most frequent propagation modeling methods.

These factors (reflection, scattering, diffraction) play a vital role in the propagation mechanism at the received terminal. Suppose a direct line-of-sight link exists between the transmitter and the radio link receiver, then the scattering and diffraction effects can be negligible. On the other hand, if the link between the transmitter and the receiver is non-line-of-sight, then the scattering and diffraction events become dominant to determine the characteristics of the propagated signals. The instantaneous received signal will change significantly when the mobile moves over short distances, resulting in “small-scale” fading. The signal is the sum of numerous contributors originating from diverse directions, and because the phases of these signals are unpredictable, the sum behaves like noise (Rayleigh fading). When the receiver moves a fraction of a wavelength, the received signal strength can

fluctuate by three or four orders of magnitude. The received signal will gradually decrease as the mobile moves away from the transmitter over longer distances. This type of received signal powder modeling is known as large-scale path loss. Large-scale propagation path loss models predict the mean signal strength for any arbitrary distance between the transmitter and receiver. As a result, large-scale propagation models can aid in determining the coverage area of a transmitter.

In this study, the experimental setup was designed to meet the investigation requirements of the large-scale path loss models in indoor campus corridors and train tunnels in South Korea.

1.3 Objectives

Considering the preceding explanation, the goal of this study is to characterize the path loss in indoor and outdoor microwave links. The objectives of this study are as follows:

Outdoor path loss due to rain

- The impacts of rainfall on four terrestrial Line-of-Sight (LOS) links have been investigated in South Korea at 18 GHz Vertical Polarization (VP), 18 GHz Horizontal Polarization (HP), 38 GHz vertical polarization over links separation of 3.2 km, and 75 GHz vertical polarization with a 0.1 km link distance.

- The experimental attenuation statistical results from the measured data are compared with different existing attenuation models. The

analysis indicates that these current prediction models do not accurately estimate the attenuation over mm-wave terrestrial links. Therefore, a simple Supervised Artificial Neural Network (SANN) approach is proposed to predict rainfall attenuation from actual atmospheric and received signal power measurements. The proposed model realizes high attenuation prediction performance.

- Experimentally measured dual-frequency attenuation datasets of terrestrial and slant links with time exceedance percentages of 0.1% and 0.01% were collected and tabulated from other investigations. Subsequently, compatible scaling techniques (frequency and polarization) that fit the collected datasets and the prediction accuracy with existing scaling techniques were studied.

- An ANN was proposed to predict the path loss due to rain using base frequency and polarization from the long-term-measured terrestrial and slant link attenuation datasets in South Korea.

Indoor corridor and tunnel path loss characterization

- The large-scale path loss coefficients of the Close-In (CI), Floating-Intercept (FI), CI model with a Frequency-weighted path loss exponent (CIF), and Alpha-Beta-Gamma (ABG) models were calculated using the Minimum Mean Square Error (MMSE)-based optimization method.

- Path losses were measured in 90 and 260 m long corridors in the university campus, and the measured path losses were modeled with CI,

FI, CIF, and ABG methods.

- The path loss was measured in a newly built train tunnel called 'Mangyang Tunnel 2' in South Korea, and the measured path losses were modeled with CI, FI, CIF, and ABG models.
- The resulted coefficients of CI, FI, CIF, and ABG models were analyzed.
- The shadow factors of the large-scale models found using the Gaussian distribution

1.4 Methodology

The indoor wireless propagation, measurements of wave propagation at S (2~4 GHz) and Ka (26.5~40 GHz) bands in extended corridors and train tunnels were campaigned in early 2021. The highlights of these investigations are:

Indoor corridor and tunnel path loss characterization

- The experiment was designed to measure the real path loss in the indoor corridor and indoor train tunnel environments at 3.7 and 28 GHz frequency bands.
- The MMSE optimization technique computed large-scale path loss models (CI, FI, CIF, and ABG) scenario-specific coefficients

- The coefficients of large-scale models, were computed with the measured path loss for the indoor corridor and indoor train tunnel environments.
- A comparative study among these large-scale path loss models was revealed through a visual graph among all considered models for indoor corridor and indoor train tunnel environments.

Outdoor path loss due to rain attenuation

- The reception and processing of the satellite beacon signals from KoreaSAT 6 at circularly-polarized beacon signals at 12.25 and 20.73 GHz were recorded.
- The received signal level of terrestrial links at 18 and 38 GHz with horizontal and vertical polarization datasets for 2013~2015 by the National Radio Research Agency (RRA) was used in the experiments.
- A new path loss model for rain was proposed with the measured data.
- In addition, a new base frequency, and polarization derived path loss model was proposed due to rain attenuation.

1.5 Thesis Layout

The dissertation is organized as follows: In Chapter 2, an overview of path loss of wave propagation in the outdoor back-haul microwave links due to rain and indoor corridors and tunnel environment due to multi-path

scattering, absorption, reflection, and were reviewed. In Chapter 3, the experimental setup of outdoor terrestrial and slant and indoor corridor and tunnels microwave links were described. In Chapter 4, path loss determination techniques based on ANN and base frequency and polarization derived techniques were discussed. In addition, the large-scale path loss techniques MMSE-based optimization coefficients are derived in this chapter. In Chapter 5, the results of (i) ANN-based path loss due to rain on outdoor (terrestrial) links, (ii) path loss due to rain on outdoor (terrestrial and slant) links derived from base frequency and polarization techniques (also called scaling), (iii) large-scale path loss for indoor corridors, (iv) large-scale path loss for train tunnel are presented. Finally, the dissertation is concluded in Chapter 6.

2. Overview of Path Loss in Outdoor and Indoor Links

In this chapter, brief path loss backgrounds in outdoor links due to rain and the techniques of determining path loss due to rain using previously known links attenuation were reviewed. Subsequently, the path loss in indoor corridors, the indoor tunnel was introduced. Then, the experimental setups were described.

2.1 Path Loss in the Outdoor Link due to Rain

The rapidly increasing demand for high data rate and capacity in wireless communications requires the use of higher frequency bands that exhibit higher bandwidth [9,10]. Therefore, microwave and mm-wave frequency bands effectively satisfy the extreme data demands for backhaul and radio access links [11]. Although higher frequency bands offer a great opportunity in terms of compact equipment and available bandwidth, they are significantly affected by atmospheric phenomena such as rain, fog, and snow, which need to be considered for network planning [12–16]. Among these impairments, rain is the primary cause of the deep fading, and network outage of radio wave links operating above 10 GHz [17, 18]. Because when a higher frequency signal propagates through the rainfall environment, its received power level significantly deteriorates owing to the impact of scattering and absorption by rainfall drop on its phase and amplitude components [10].

Hence, it is crucial to study rain attenuation over higher operating frequencies and shorter distances proposed for 5G and beyond.

Several researchers have developed rain attenuation prediction models for terrestrial links in recent years. The critical input parameters adopted for most of these techniques are the point rainfall rate and specific rain attenuation reproduced by the link length L, which is well-adjusted by a reduction factor that considers the space diversity of rainfall along the path [12, 14, 15, 19]. In addition, although mm-wave bands at shorter distances are a promising solution for 5G and beyond, most of the existing rain fade prediction models were developed for operating frequencies less than 30 GHz and link separations more than 10 km [9]. Furthermore, most of these methods, including the ITU-R [19], are semi-experiential with limited accuracy and irregular behaviors, particularly for locations different from the actual measurement locations. The limited accuracy and irregular behaviors occur owing to the absence of a sufficient database and human capability to derive an empirical formula that correlates the complex input features [20–23]. Therefore, devoted experiments are necessary to validate the precision of these existing models and propose alternative rain attenuation prediction methods over short link distances and high-frequency bands.

Currently, deep learning is garnering considerable attention for analyzing the complex connection between its input factors and the predicted output (target) [24]. Specifically, a Supervised Artificial Neural Network (SANN) with hidden nodes can indicate the relationship within their given ranges [20]. In this regard, ten different emerging learning-based models of rain attenuation are surveyed in [25]. Consequently, this study attempts to

elucidate further the impacts of rainfall on radio links at K, Ka, and E-bands in South Korea.

Selected Existing Rain Fading Models

Rainfall significantly influences radio wave propagation, especially at mm-wave and microwave frequencies. In addition to the rainfall rate, link length, carrier frequency, and type of polarization play significant roles in planning terrestrial networks. Recent research has proved the use of rainfall attenuation relationships in predicting rainfall rate due to the significant linkage between rainfall rate and rain attenuation [26–28].

Researchers have developed numerous fade estimation models to evaluate rainfall attenuation over different regions of the world [29–31]. The most famous and preferred model used in the various regions is the distance factor developed by ITU-R [23]. Although the ITU-R method can be implemented to derive rain attenuation for horizontal variation, it may not be the best employable model in all regions. Therefore, several techniques have been proposed and developed to estimate rain attenuation using the path reduction factor, for example, Lin's model [32], and the RSM model [33]. Most of these models require the CCDF of the rainfall rate at 0.01% of time exceedance.

The general formula for rain attenuation prediction [34] at different percentage of time exceedance $\mathrm{A_p}$(dB) can be calculated as in (2.1):

$$A_p(dB) = xR_p{}^y \times r \times d \tag{2.1}$$

where R_p is the rain rate with p percentage of time exceedance, x, and y are

regression coefficients that refer to the specific rain attenuation (dB/km), r is the path length reduction factor, and d is the link length.

Furthermore, calculations on specific rain attenuation, effective path length, and total rain attenuation overall effective path length have been derived, as introduced by ITU-R [29], and three frequently used rain attenuation predictions with better performance [35] are revised in the following subsections.

ITU-R Model

Rainfall attenuation for terrestrial LOS radio links can be calculated using a disdrometer by multiplying specific attenuation by effective path distance [34]. Hence, the ITU-R P.530-17 [19] presents the determination of rainfall attenuation exceedance $A_{0.01}$(dB) at 0.01% of time exceedance, for the terrestrial links, as expressed in Equation (2.2):

$$A_{0.01}(dB) = A_{sp} r d \tag{2.2}$$

where $A_{0.01}$(dB), A_{sp}, d, and r represent rain attenuation, specific rain attenuation, path length, and reduction factor as defined in Equation (2.3).

$$r = \frac{1}{0.477 d^{0.633} R_{0.01}^{0.073a} f^{0.123} - 10.579(1 - e^{-0.024d})} \tag{2.3}$$

The maximum suggested value by ITU-R for r was 2.5. However, using Equation (2.3), the value of r in this study at a 75 GHz frequency and 0.1-km link length is 4.622, which is greater than 2.5. Consequently, at the mmWave

carrier frequency, the value of r increases as the link distance decreases [14], [20]. For a very short link distance (<300 m), the value of r exceeds 2.5, which is not recommended [19]. Recently, a modification of distance factor r was proposed in [36] for link distance, d < 1km and frequency, f > 40 GHz. However, his proposed modified r is not optimal in our 75 GHz frequency with a 0.1 km link length. Again, the specific attenuation owing to rain is determined from the rainfall rate using the following power-law relationship [37–39].

$$A_{sp}(dB/KM) = xR_{0.01}^{y} \tag{2.4}$$

where $R_{0.01}$ is the rain rate, and x and y are regression coefficients that depend on several factors, such as polarization, carrier frequency, temperature, and raindrop size distribution [37]. These values of x and y can be experimentally determined as empirical values. The ITU-R P. 838-3 [39] provides the prediction values for x and y for the 1~100 GHz frequency bands for horizontal and vertical polarization.

Lin Model

The path reduction factor technique was proposed by Lin [32], as expressed in Equation (2.5):

$$r = \frac{1}{1 + [d/d(R)]} \tag{2.5}$$

where $d(R)$ is defined by Equation (2.6).

$$d(R) = \frac{2632}{R - 6.2}, \text{ for R} > 10\,\text{mm/h} \tag{2.6}$$

where r, d, and d(R) represent the reduction factor, path length, and characteristics path length defined in Equation (2.6).

Revised Silva Mello Model

Another path reduction model proposed by Silva Mello [33] is expressed by Equation (2.7):

$$r = \frac{1}{1 + [d/d_0(R_p)]} \tag{2.7}$$

where R_p and d_0 represent the rainfall rate at p percentage of time, and cell diameter, respectively. The cell diameter, d_0 is given by Equation (2.8):

$$d_0 = 119R^{-0.224} \tag{2.8}$$

In our experiments, the values of r according to Lin's model [32], and the revised Silva Mello model [33] are nearly equal to those of 18, 38, and 75 GHz frequencies. As a result, it indicates that r does reduce the distance. Hence, the Revised Silva Mello (RSM) and Lin models exhibit a high underestimation of attenuation compared to the measured one.

2.2 Rain-derived Path Loss in the Outdoor Link: based on the base Frequency and Polarization

Rainfall is a notable impediment to the transmission of mm-wave signals from the transmitter to the receiver. Raindrops can absorb, disperse, depolarize, and diffract the propagated wave [29]. In [25], 17 parameters have been listed that causes rain attenuation. All these parameters (or most

significant) are used to input a rain attenuation predictive model called the rain attenuation model, where attenuation is output. As per recent literature, determining path loss due to rain using previously known links attenuation (also called 'scaling' in short) properties have been developed for four parameters: frequency, path length, polarization, and elevation angle. Consequently, considering the scaling-related parameters, rain attenuation (A) can be expressed as (2.9):

$$A \equiv A(L, f, \theta, R, \text{polarization}) \tag{2.9}$$

where L–path length in the rain, f–operating frequency, θ–elevation angle, and R–rainfall rate. However, scaling of the rain attenuation model for these parameters has not yet been developed. Among these parameters, four parameters: frequency, elevation angle, path length, and polarization scaling techniques are proposed in the literature. Mathematically, scaling can be defined as:

$$A_{f_2} = g(A_{f_1}) \tag{2.10}$$

$$\begin{cases} A_V = g(A_H) \\ A_H = g(A_V) \end{cases} \tag{2.11}$$

where g: is the function that defines mappings of attenuation for frequency and polarization; A_{f_2}–attenuation at frequency f_2; A_{f_1}–attenuation at frequency f_1; A_H–attenuation at horizontal polarization; A_V–attenuation at

vertical polarization. It is possible to determine the rain attenuation for another frequency using Equation (2.10). Likewise, using Equation (2.11), it is possible to determine the rain attenuation for vertical or horizontal polarization with the condition that the corresponding horizontal or vertical attenuation is known. In the next section, ITU-R implementations of the Equations (2.10) and (2.11) for terrestrial and slant links will be discussed.

Rain attenuation models for frequency scaling are applicable if a different frequency signal passes through the same storm. It is helpful to measure the amount of rain attenuation that occurs at a given frequency. For example, it is helpful to have experimental results available at one frequency to estimate the rain attenuation at another frequency. Furthermore, frequency scaling techniques can help quickly predict rain attenuation at different frequencies. The application of frequency scaling can help determine the projected attenuation in a dual-frequency use of satellite communication or predict attenuation at different frequencies [40, 41]. Most of these scaling techniques were derived for slant links. As said earlier, scaling methods can help plan the link budget and fade mitigation technique applications over terrestrial links. In the literature, researchers have made efforts to find accurate frequency scaling techniques. These efforts are based on different methods, such as empirical formula [19, 42], consideration of the correlation between peak rain rate and corresponding attenuation [43], development of a line on a map that links points that have the same meteorological incidence called isopleths [44], the path-averaged raindrop size distribution [43], and rain inhomogeneity factor [45]. The ITU-R model can be used to predict frequency scaling as given by Equation (2.12) [19, 42]:

$$A_2 = A_1 \left(\frac{\Phi_2}{\Phi_1}\right)^{1-H(\Phi_1,\Phi_2,A_1)} \tag{2.12}$$

where A_1 and A_2 are the rain attenuation at frequencies f_1 and f_2 (GHz), respectively; $\Phi(f)$ and H are defined by Equation (2.13), (2.14) and Equation (2.15), respectively.

$$\Phi_1(f) = \frac{f_1^2}{1 + 10^{-4} {f_1}^2} \tag{2.13}$$

$$\Phi_2(f) = \frac{f_2^2}{1 + 10^{-4} {f_2}^2} \tag{2.14}$$

$$H(\Phi_1, \Phi_2, A_1) = 1.12 \left(\frac{\Phi_2}{\Phi_1}\right)^{0.5} (\Phi_1 A_1)^{0.55} \tag{2.15}$$

The applicable frequency of this model is limited to 7~55 GHz for slant path application [42] and 7~50 GHz for terrestrial path application [19].

Polarization is the direction of the electric field in an electromagnetic wave. The commonly used polarization of radio waves is vertical, horizontal, right-hand circular, and left-hand circular. The ITU-R model P.530-17 [19] can predict the attenuation for vertical polarization, given that long-term attenuation statistics exist at a horizontal polarization and vice versa for a given terrestrial link. Mathematical formulas (Equations (2.16) and (2.17)) to determine the polarization conversion are given in [19]. The limitation of this model is that it does not apply in the case of circular polarization. According to [19], the rain attenuation of horizontal to vertical and vertical to horizontal polarization can be determined by:

$$A_V = \frac{300A_H}{335 + A_H}(dB) \tag{2.16}$$

$$A_H = \frac{335A_V}{300 - A_V}(dB) \tag{2.17}$$

where A_V and A_H are the attenuations due to vertical and horizontal polarization, respectively, and the frequency limit is 100 GHz. It is assumed to be valid in all parts of the world and path lengths up to 60 km.

Discussion on ITU-R Model: South Korea Perspective

The frequency and polarization scaling performance can be measured through available multi-band operating frequency attenuation datasets of different propagation measurement campaigns. To do so, some experimentally measured attenuation datasets around the world to assess the performance of the ITU-R model in predicting the frequency and polarization scaling were collected. A limited number of such multi-band operating frequency campaigned rain attenuation measurement information for terrestrial and slant links were found. The collected datasets are given in Tables 2.1 and 2.2, where Table 2.1 corresponds to terrestrial links, and Table 2.2 corresponds to slant links. The '(a)' section contains the collected datasets in both tables. To emphasize the maximum availability of the radio links and the corresponding attenuation at 0.1% and 0.01% time exceedance, and corresponding to the typical link availability of 99.9% and 99.99% over time, were tabulated. The '(b)' section of Tables 2.1 and 2.2 contains some processed datasets: predicted attenuation, which is determined through the scaling prediction

models and error in prediction, computed by Equation (2.18):

Table 2.1: Path loss prediction through frequency scaling of terrestrial links.

		(a)				(b)	
	Ref.	F_1 (GHz)	F_2 (GHz)	A_1 (dB)	A_2 (dB)	ITU-R [19]	Error% [19]
0.1%	UK [46]	36	55	8	12	14	17
	Malaysia [36]	26	38	4.8	5.5	9	64
	Italy [9]	73	83	1.66	2	2	0
	Korea [47]	73	83	12	8	13	63
	Measured	18	38	8	16	26	63
0.01%	UK [46]	36	55	18	22	28	27
	Malaysia [36]	26	38	11	15	19	27
	Italy [9]	73	83	24	24	26	8
	Korea [47]	73	83	4	4.2	4.5	7
	Measured	18	38	17	41	48	17

$$\text{Error } \% = \frac{A_p - A_m}{A_m} \times 100[\%] \tag{2.18}$$

where A_p is the predicted attenuation, and A_m is the measured attenuation. A description of Tables 2.1 and 2.2 is provided subsequently:

In Table 2.1, some dual frequency-based experimental measured datasets are presented, and the frequency scaling of ITU-R P.530-17 is evaluated. The table shows the prediction error using the ITU-R [19] of terrestrial links with rain exceedance percentages of 0.1% and 0.01%. It is worth mentioning that, in radio network planning, the percentage of time exceedance helps determine the link budget availability in horizontal and slant link designs. The availability indices used in link budget planning are typically 0.01 percent

Table 2.2: Path loss prediction using frequency scaling of slant links.

		(a)				(b)	
	Ref.	F_1 (GHz)	F_2 (GHz)	A_1 (dB)	A_2 (dB)	ITU-R [42]	Error% [42]
0.1%	Japan [40]	12.65	18.9	10	20	21	−5
	Darmstadt [48]	12.5	20	6	12	14	17
	Darmstadt [48]	20	30	12	24	23	−4
	Virginia Tech [49]	20	30	12	25	23	−8
	Measured	19.8	20.73	13	12	14	17
0.01%	Japan [40]	12.65	18.9	14	24	28	17
	Darmstadt [48]	12.5	20	11	27	25	−7
	Darmstadt [48]	20	30	27	51	47	−8
	Virginia Tech [49]	12	20	12	29	29	0
	Virginia Tech [49]	20	30	29	44	50	14
	Measured	19.8	20.73	25	18	27	50

of the time exceedance used as link budget fade threshold. The attenuation may lead to network outage above 0.01% of the time exceedance. According to Table 2.1, the measured dataset in Italy showed comparatively good performance to predict attenuation at 83 GHz from the 73 GHz measured dataset.

While the dataset in Korea from different two experimental results ([47] and measured data by the National Radio Research Agency (RRA) [50]) does not agree well with the ITU-R P.530-17 model, with showing errors of 63% (at 83 GHz) [47], and 63% (at 38 GHz) for measured data by RRA [50].

The relative errors due to frequency scaling of ITU-R P.618-13 model

of slant links with rain times exceeding 0.1% and 0.01% are shown in Table 2.2. This table shows that the predicted error performance of the ITU-Rmodel [42] offers good prediction ability for the data measured at Darmstadt [48] and data measured by Virginia Tech [49] at 20 GHz. On the other hand, the measured results in Korea showed a comparatively higher error generated by the ITU-R P.618-13 model.

2.3 Path Loss in the Indoor Corridor

By 2023 there will be over three times as many devices linked to the internet protocol network as the world population [51]. Humans will use many devices to access multimedia content, services, and data [52] through the wireless network. One of the most effective decisions to facilitate Enhanced Mobile Broadband (eMBB) service to these huge devices is to relocate data transmissions into an underutilized nontraditional range, where huge bandwidths are available [53]. 5G-new radio addresses high data rates service, which is achieved by the maximum spectral efficiency [54] and use of Millimeter-Wave (mmWave) [55]. With the large bandwidth within the mmWave spectrum, a significant component of the 5G mobile network the mmwave has been proposed to enable multi-gigabit telecommunication, visual services, for example, ultra high definition video and high-definition television [56–59] and multi-gigabit communication, like device-to-device communication [57, 60, 61]. A large part of all the eMBB services will be in the indoor environment, where human stays for different activities like studying, working, living, entertaining, or healing purposes.

Presently, 5G primary service locations with high-frequency bands are

anticipated to be environments such as internal hot-spots and micro-cells [5]. However, the mmwave frequency band suffers from high building penetration loss and more significant delay spread in outdoor to indoor coverage networks as reported in [1–4]. Consequently, a separate indoor transmission system can promise to ensure better spectral efficiency (and better eMBB services) for indoor network demands. However, only deploying different transmitters inside the indoor will not be helpful if proper transmission of the electromagnetic wave is not modeled according to its internal infrastructure settings and the used materials [6]. Therefore, it needs to find a proper propagation model matching its structure, which can help achieve high-speed data transfer service as per the demands for indoor users.

Indoor mmwave propagation path loss models are critical components to ensure quality network access for indoor environments [62]. Consequently, path loss modeling for indoor users is vital to network design, planning, performance evaluation, and implementation. Therefore, several organizations [63, 64] are now designing mmwave channel models.

Path loss modeling is a mathematical analysis of the radio wave propagation process that considers the signal-to-noise and interference ratios and spectral efficiency to provide the network coverage area [65]. Besides, as the mmwave band is the most promising carrier in wireless propagation channels and has higher wall penetration loss, precise path loss models are required [62]. Therefore, several path loss models based on the statistical or empirical approach, such as the Okumura–Hata models [66], the European Cooperation in Science and Technology (COST) 231 path loss models [67] that consider the number of traversed floors, number of lightweight interior

partitions, windows, and the number of concrete or brick internal walls [67], and other models [68,69], are proposed in the literature. Most of these models consider the attenuation due to individual elements that hinder the radio wave propagation. Nevertheless, recently, large-scale attenuation parameters have been realized for the propagation modeling of the radio wave in indoor environments, rather than considering the attenuation due to individual elements [65, 70–72].

In the CI, FI, CIF, and ABG model, some parameters related to the path loss function of either distance, frequency, or distance and frequency parameters. In such a model, the path loss and the parameters' dependency can be realized through coefficients like 'path loss exponent,' 'α,' and 'β' [73]. In many respects, the indoor environment differs substantially from the outdoor environment [6]. As a result, interior path loss models must account for changes in floor layout, construction materials, the variety and quantity of office equipment, numbers of persons and their movements, and the density of utilizing the wireless network in the vicinity. Furthermore, multi-path propagation and normal fading and path loss due to distance and physical phenomena such as interference, reflection, refraction, dispersion, and penetration can affect the received signal's characteristics [74].

In the literature, investigations on radio wave propagation have been studied either using the measured experiment setup condition [65, 70, 71, 75] or via a simulation-based study [76]. However, in both types of analysis, currently, the maximum path length in the corridor environment studied in [77] and about 100 m. In [75], a total 77 m path length has been studied, but 25 m was Non-Line-of-Sight (NLOS) path length in an 'L-shaped' cor-

ridor. As previously noted, several initiatives have been undertaken in the literature to assess path loss in indoor corridor environments. Among these studies, more than 30 m corridor length measurement results are reported in [70, 71, 76–86]. In Table 2.3, all of these research outcomes' investigated link types, frequency bands, and distance studied were presented.

Table 2.3: Propagation study for the path length in the corridor more than 30 m.

Ref.	Link	Freq. (GHz)	Dist. (m)
[76]	N/LOS	60	30
[70]	N/LOS	14/22	30
[78]	LOS	39	5/50
[79]	LOS	28	1/60
[80]	N/LOS	60	2.4/60
[71]	N/LOS	26/32/39	65
[81–83]	N/LOS	28/38	1/67
[84]	N/LOS	41/0.5	1.35/70
[85, 86]	N/LOS	60/74	10/80
[85]	N/LOS	30	10/80
[77]	N/LOS	28	<100
This work	N/LOS	3.7/28	90/260

New York University (NYU) and the Mobile and wireless communications Enablers for Twenty-Twenty Information Society (METIS) have reported ongoing campaigns to estimate 5G channels and modeling for the 20~70 GHz range [11, 87]. Most research recently concentrated on the 28, 38, and the 81~86 GHz E-band [62]. However, several research outcomes are available at 3.7 and 28 GHz [77, 79, 81–83] bands, which are not significant enough, and there is still research scope to find suitable path loss models in different environments at these frequency bands. The above-stated indoor

radio wave propagation prediction differs in certain respects from the outdoor one [6]. The extent of network coverage is determined in the indoor instance by the construction geometry, and the boundaries of the structure itself affect radio wave propagation [88, 89]. Frequency reuse between floors of the same building is typically wanted, adding a third dimension to interference difficulties. Small changes in the immediate radio path environment may significantly influence propagation features [90]. Consequently, detailed structural variation-based indoor corridor propagation modeling is also necessary.

The 3.5 GHz bands are currently in the roll-out operation with the 5G network in Korea, and 28 GHz bands are probable future frequency bands to be deployed in Korea [91] and the USA [92]. So, this study designed an experiment to study the path loss at 3.7 and 28 GHz frequency bands in the long indoor corridors that were not explored yet.

2.4 Path Loss in the Indoor Train Tunnel

The usage of tunnels increases rapidly with the pace of human living standard development for many purposes such as transportation, mining, natural fossils, minerals, or military operations. Among these tunnels, train tunnels have become essential with modern civilization. Consequently, deploying a 5G network inside the tunnel is critical to ensure security, safety and increase the efficiency of train operations [93].

A reliable transmission is intended to achieve a stable and efficient telecommunication facility between the transmitter and the receiver. Path loss is one of the most significant features which several elements may impact, such as

signal frequency, distance from source to destination, environmental condition and the effect of signal fading, and weather conditions [82]. Many studied models of various propagation pathway loss for multiple interference and noise-limited settings were investigated in numerous ways to address the wireless network's random character [55].

On the other hand, the knowledge of radio propagation inside the tunnel is essential for setting up the transmitter and receiver and satisfying the system specifications. For instance, statistical features of the wireless channel are significant for defining transmitter and receiver characteristics and for the budget link computation, such as the probability density function of the received signal intensity and fade duration. In addition, these radio propagation models typically predict path loss, power delay profile, or delay spread for specific transmitter and receiver locations [94]. As mentioned earlier, the propagation inside the tunnel is different compared to other sorts of propagation media such as outdoor, outdoor to indoor, indoor to outdoor, or indoor to indoor radio wave propagation [95]. The main difference is that in the tunnel, the radio wave is enclosed by the blocking surface (of the tunnel) through which the refracted wave can not reach the receiver, as such propagated signal is received in other cases through a penetration loss, the tunnel blocking plane. Consequently, the propagation of radio waves inside the tunnel needs to pay attention to separately.

The properties of the wireless propagation channel define the ultimate achievement of the required quality of service in a wireless telecommunication network. The actual realization of wireless propagation channels in a real tunnel environment is consequently quintessential. Several channel

dimensions have been carried out in various tunnels [96–98]. Unlike open-air propagation, tunnel propagation includes electromagnetic waves in an enclosed environment [99]. A leaky feeder communication system can be deployed inside confined locations and, more precisely, to road or rail tunnels [95]. The cable is 'leaky' in the sense that it includes gaps or slots in its outer conductor that allow radio signals to leak into or out of the cable along its entire length. Because of this signal loss, the line amplifier must be installed regularly to boost the signal back to acceptable levels, which results in significant weight and cost increases [100]. However, inside the tunnel, there is a high chance that the cable can be damaged, which may cause communication complications in the entire tunnel. Consequently, 'leaky feeder' is not generally deployed for telecommunication purposes inside tunnels.

At present, 'modal expansion' in tunnels or corridors is used for a standard approach of wave propagation analysis [94, 101–103]. In the 'modal expansion' approach, a tunnel is considered an empty wave-guide, and the field in the cross-section is represented as a sum of the transverse Eigenvalues above the cutoff frequency. However, the method becomes useless at high frequencies such as the millimeter wavelength. Because the dimensions of the transverse wavelength are far broader, and too many modes are needed to be considered. The computation is incorrect in the modified case, and the modal method is no longer effective.

The radio wave propagation modeling inside the tunnel can be done through the solution of electromagnetic waves by numerical methods. The numerical approach of finding radio wave propagation inside the tunnel is comparatively complex and needs a considerable computing capacity. Conse-

quently, there are several simplified techniques to reduce the computational complexity is proposed in the literature: Finite Difference Time Domain (FDTD) [104], Crank Nicolson (CN) method [105], Vector Parabolic Equation (VPE) [106,107], Scalar Parabolic Equation (SPE) [106], Uniform Theory of Diffraction (UTD) [108–110]. All these simplified techniques suffer from some disadvantages, such as the FDTD method being limited to the large-sized tunnel, and the primary constraint of CN is the need to resolve sets of simultaneous equations that might grow to be too big to tackle dense mesh issues efficiently. The VPE technique assumes fields travel within 30° in the propagation direction, the scalar PE can only be used for tunnels with Perfect Electrical Conductor (PEC) walls, and UTD can not be used for the junction where tunnels are not crossed perpendicularly.

Another well-known path loss modeling in the tunnel can be implemented by the Ray-Tracing Technique (RT). However, this technique has several limitations on implementing or analyzing the RT signals. For example, an implementation through Delay Line (DL) time-domain analysis is minimal if the minimum delay is less than 8 ns (in that case, it will require larger Bandwidth (BW), for example, with 1 ns Tapped Delay Line (TDL), it will need 1 GHz BW) [111]. Another implementation is through the Shooting Bouncing Ray Tracing (SBRT) realization technique, and this approach has the difficulty of the size of the receiver hypothetical size to receive the propagated ray [112, 113]. Another implementation of RT is through 3-D ray-tracing modeling, which is challenging to obtain convergence results as there are many reflections [114].

Consequently, the modal expansion, numerical approach, and RT-based

technique of wave propagation of the tunnel have many challenging issues. On the other hand, a large-scale path loss model was applied to model wave propagation in tunnels [115], and the results indicate that the large-scale path loss models can be deployed to model radio wave propagation inside the tunnels. Large-scale path loss models have been used to model indoor corridors [65, 70] and stairwells [116]. Consequently, large-scale path loss models were used to model measured data, and the results were satisfactory.

3. Experimental Setup

The actual path loss was measured to characterize wave propagation in outdoor and indoor microwave links. This chapter describes the measuring technique, description of the channel formation, measurement environment description, instruments used for the measurement campaign, and the signal pre-processing steps.

3.1 Experimental Setup: Terrestrial Links

The measurements of the received signal level (RSL, dBm), raindrop size (mm), and rainfall rate (mm/h) were conducted for the four links located in Icheon, South Korea, as illustrated in Fig. 3.1. Three links operating 18-GHz horizontal polarization, 18-GHz vertical polarization, and 38-GHz vertical polarization with link length of 3.2 km were located between Icheon tower 37°8′49.57″S 127°32′54.82″E (RRA station) and Khumdang tower 37°8′8.41″S 127°30′56.16″E KT station). The fourth link operating at 75 GHz in vertical polarization with a link separation of 0.1 km is located between Dong Yoksang's station 37°11′49.2″ S 127°25′33.6″E, and the same Icheon tower of the first links shown on the right side of Fig. 3.1. Fig. 3.2 shows the bird's eye view of the experimental scenario. The front feed parabolic antennas used in these experiments were randomly covered to minimize wet effects. The main link parameters for the four operating frequencies are summarized in Table 3.1.

In addition to the received signal power measurement of the links, the

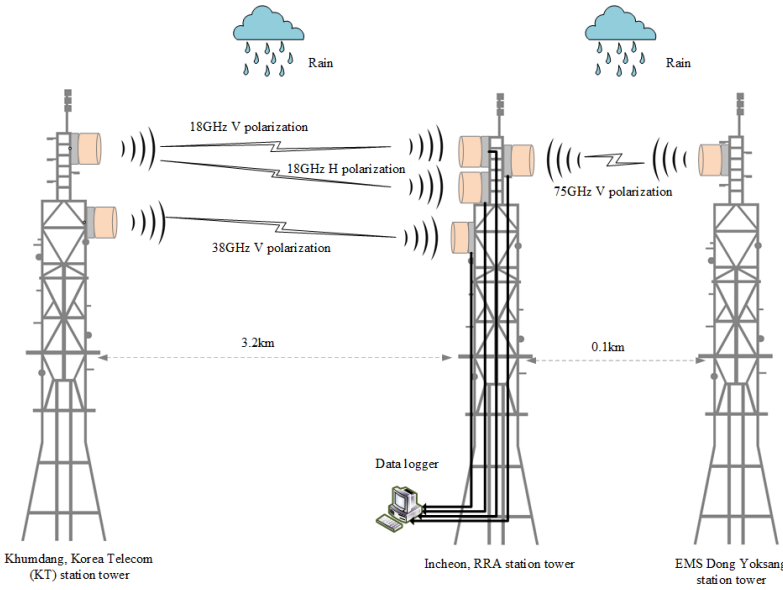

Figure 3.1: Measurement scenario of the experimental terrestrial link.

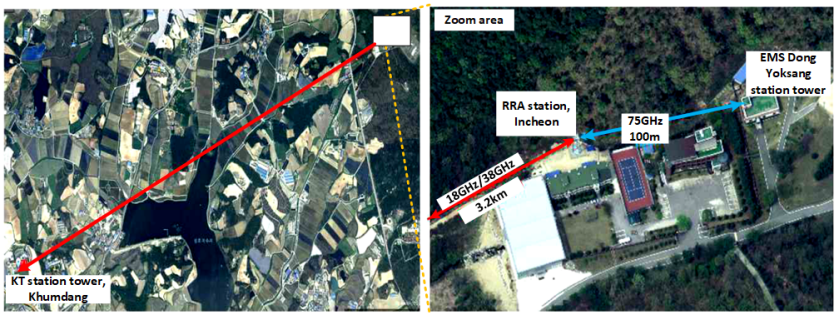

Figure 3.2: Bird's eye view of the measurement campaign of terrestrial link.

three-year rainfall rate, raindrop size, and other atmospheric elements were measured simultaneously. The rainfall data were collected by OTT Parsivel at a 10-s time interval according to the detailed procedures discussed in [117]. Meanwhile, RSL measurements at a 10-s integration time for the above links were conducted as described in [117]. The corresponding rain attenuation from RSL is obtained by determining the differences between

Table 3.1: Summary of the main link parameters descriptions.

Description	18 GHz VP	18 GHz HP	38 GHz	75 GHz
Antenna type	parabolic	parabolic	parabolic	parabolic
Frequency band (GHz)	17.7~18.2	17.7~18.2	38.3~38.9	71~76
Polarization	VP	HP	VP	VP
Max. transmit power	22 dBm	22 dBm	18 dBm	7 dBm
Modulation type	QPSK	QPSK	QPSK	QPSK
Spectral efficiency	8 bit/Hz	8 bit/Hz	8 bit/Hz	6 bit/Hz
BER received threshold (dBm)	-32.8	-52.34	-29.88	-22.95
Half power beam width	1.9°	1.9°	0.9°	0.8°
Antennas size (m)	0.6	0.6	0.6	0.6
Gain (dBi)	38.8	38.8	45.1	45.1

the RSL measured during rainy and non-rainy conditions, as expressed in Equation (3.1).

$$R_A(\text{dB}) = \text{RSL}_{\text{no}-\text{rain}} - \text{RSL}_{\text{rain}} \tag{3.1}$$

where R_A(dB), $\text{RSL}_{\text{no-rain}}$ and RSL_{rain} represent rain attenuation, RSL during no rain, and RSL during rain, respectively.

3.2 Experimental Setup: Slant Links

Propagation measurements over an earth-space path were performed at Mokdong-13 na-gil (37.545903° N, 126.883° E), Yangcheong-gu, Seoul, the Republic of Korea by the RRA [50]. The experiment campaign received Ku and Ka-band signals through the earth station facility installed on the Korea Radio Promotion Association building rooftop, pointing toward Koreasat 6 satellite, at 12.25 and 20.73 GHz. Both of the receivers sample the data at

a 10-second interval. Satellite links were 99.95% available, and the scheme for setup is shown in Fig. 3.3. Furthermore, an optical disdrometer records the rainfall rates with satellite signal monitoring for all satellite links. As shown in Fig. 3.3, the parabola offset antenna faces Koreasat 6. Detailed antenna specifications are given in Table 3.2. In addition, a separate low noise block converter was added for the circularly polarized beacon signal at 12.25, 20.73 GHz of Koreasat 6. Attenuation due to rain is calculated by finding the difference between the RSL during clear sky conditions and RSL during rain as Equation (3.2). Details of the experimental setup are discussed in [118].

$$\mathrm{A(dB)} = \mathrm{RSL_{clear\ sky}} - \mathrm{RSL_{rainy}} \tag{3.2}$$

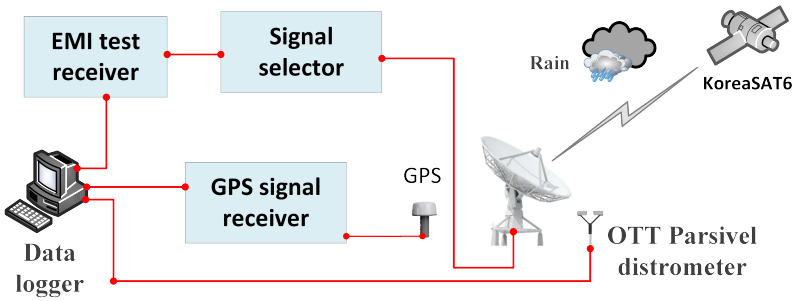

Figure 3.3: Experimental setup for rain attenuation and rain rate measurement (slant links); the figure is not drawn to scale. [Global Positioning System (GPS), Electromagnetic Interference (EMI)].

3.3 Measurement Campaign in the Indoor Corridors

This section describes the channel sounder and the scenarios incorporated in the measurement operations. M5183B keysight signal generator (at Tx

Table 3.2: Specifications of the 12.25 and 20.73 GHz links for Koreasat 6 satellite link [50, 117].

Parameters	**Quantity**
Elevation angle	45°
Azimuth angle	197.5°
Sea level (km)	0.055
Antenna type	Offset parabolic
Frequency band (GHz)	10.95~31
Beacon signal level for clear sky at 12.25 GHz	−80.5 dBm
Beacon signal level for clear sky at 20.73 GHz	−38.7 dBm
Polarization	Circular
Gain	55 dB ± 2 dB
Type	OTT
Measuring area	54 cm^2

side), keysight PXI 9393A signal analyzer (at Rx side), and two-directional horn antennas were used along with other devices. The channel sounder and the utilized other devices in the measurement campaign are shown in Fig. 3.4. A clean and accurate alternative to the analog PSG is the N5183B MXG (PSC and MXG are product series names of Keysight Technologies, Inc.) microwave analog signal generator with benefits in size and speed. It can yield the required purity of spectra precisely, the desired output power level. In addition, the device is compact with just two racks of units and yet can maintain rigorous performance with near-PSG performance levels. The module can also be used to test radar modules and methods giving best-in-class state noise of ≤ -124 dBc/ Hz(10 kHz offset) with -75 dBc spurious (at 10 GHz). The use of the MXG can further expedite the calibration process with a best-in-class switching rate of about 600 μs.

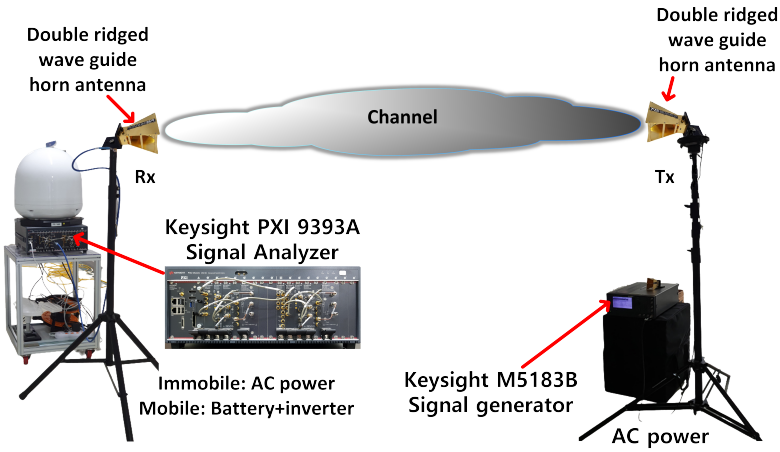

Figure 3.4: Channel sounder architecture.

The measurement campaign used keysight's MXG N5183B signal generator as a transmitting source. In the receiver end, keysight's signal analyzer PXI 9393A was used to receive and process the received signal, operating in the frequency range of 9 kHz~50 GHz. Horn antennas with gains of 10, 20, and 20 dBi were employed in the experimental setup for the 3.5 GHz directional antenna, 28 GHz directional antenna, and 28 GHz TAS antenna, respectively. H-H co-polarization was used for the horn antennas and throughout the measuring experiments. Fig. 3.4 provides the measurement system with the elements, and Table 3.3 shows the additional operational parameters of the system.

3.3.1 Signal Generators

The transmitter (MXG N5183B) can generate Continuous sinusoidal Wave (CW) analog signals and can generate a wide range of signals from 9 kHz to 40 GHz [119]. The frequency switching can be implemented us-

Table 3.3: Specifications of the channel in the corridor.

Parameters	3 GHz	28 GHz	28 GHz TAS
Operating freq. (GHz)	3.7	28	28
Bandwidth (MHz)	1	1	1
Tx antenna	horn	horn	horn
Rx antenna	Double ridged horn,gain:10 dBi	20 dBi WR28 Standard horn	20 dBi WR28 standard horn, 16×2 array
LNA gain (dB)	57	57	57
System gain (dB)	40	40	40
Tx antenna height (m)	1.75	1.75	1.75
Rx antenna height (m)	1.5	1.5	1.5
Rx antenna gain	10	20	20
Beam-width	45~45°	18~21°	18~21°
Polarization	HP	HP	HP
Tx cable loss (dB)	2.8	9.4	9.4
Rx cable loss (dB)	2	6.2	6.2

ing a 'listing mode' type operation where the switching time is 600 μs. The sweep mode is also 'listing type' as a frequency switching technique, changing stepwise. It can generate the minimum power –130 dBm, and the maximum power can be +20 dBm (say at 1 GHz). The signal generator has a level accuracy of about ±0.7 dB. In the Single-Sideband (modulation) (SSB) mode operation, the phase noise can be at 1 GHz with a 20 kHz offset setting is –124 dBc/Hz. It can generate harmonics at 1 GHz up to –55 dBc, and non-harmonics (at 1 GHz) up to –100 dBc. Furthermore, it can generate ten ns pulse width and pulse modulation phase deviation (maximum in standard mode) in the range of 0.5~64 rad.

3.3.2 Signal Analyzer Properties

The vector signal analyzer's core comprises the following components: M9308A PXIe synthesizer, M9365A PXIe down-converter, and M9214A PXIe Intermediate Frequency (IF) digitization. PXI 9393A [120] signal analyzer was used in the measurement campaign. This device can be used to analyze the frequency range from 9 kHz to 8.4, 14, 18, or 27 GHz and in an extended mode from 3.6~50 GHz. It can analyze the signal with 40, 100, or 160 MHz. The absolute amplitude accuracy is ±0.13 dB, and the frequency switching is approximately smaller than 135 µs. It can display an average noise level up to -168 dBm / Hz. The third-order inter-modulation is about +31 dBm.

3.4 Measurement Scenario Description

3.4.1 Corridor Wall and Floor Materials

The measurement operations were conducted inside the Chosun University (CU), in the 10^{th} straight floor corridor of the IT convergence building and the straight corridor of the main building. The indoor ambiance restrained the signaling system and directed it to different directions that affected the electrical phenomena of the received signal. Several small fire extinguishers, a hot and cold drinking water supply system, and an automatic drinking beverage dispenser made of metal were located in the extended portion of the corridor in the middle of the IT convergence building. The hallway comprises brick walls, a square-tiled floor, metal doors, and metal grill structures to hold the glass at the two long corridor ends. The sidewalls of the IT convergence corridor are constructed of lightweight concrete and

a false gypsum ceiling. The rooms of the IT convergence building consist of metal doors, light cement walls, and glass windows located on the outer sidewall only.

3.4.2 Corridor Shape Irregularities

There are four irregular spaces in the IT corridor. These irregular spaces were marked by circled numbers, shown in Fig. 3.5. In the middle of the IT corridor, there are spaces on both sides of the corridor. At one side, there is a space to accommodate a 'beverage vending machine,' and at another corner, there is a drinking water purifying system (see around ③ of Fig. 3.5). On the other side, there are spaces for two elevators on one side, and on the other side, there are emergency stairs (see around ② of Fig. 3.5). Another irregularity of the corridor is the restroom spaces marked by the place around ⑥ of Fig. 3.5. The fourth irregularity was the place market by space around ⑧ of Fig. 3.5, located behind the transmitter during the measurement operation. Also, in the main building corridor, one side was mainly open, and another side was the classroom, research lab, and office shown in Fig. 3.6.

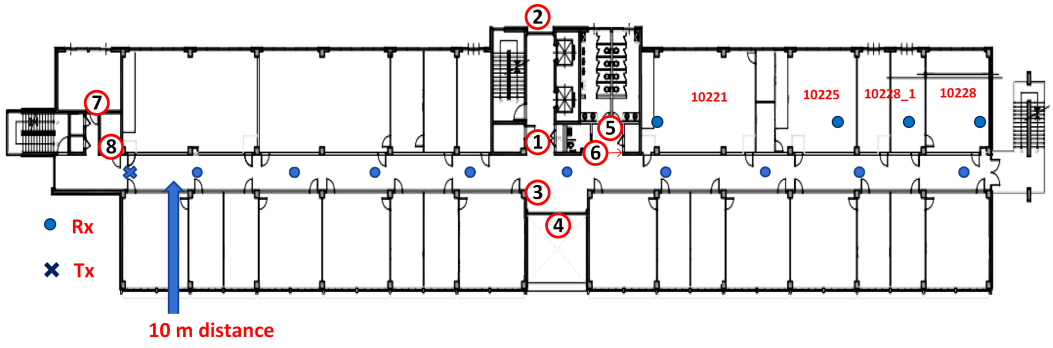

Figure 3.5: Architectural drawings of the 10th floor IT building corridor.

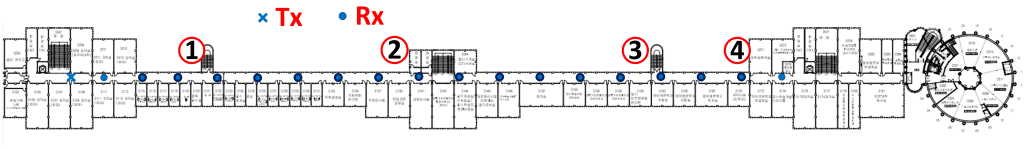

Figure 3.6: The experimental outlet is on the 3rd floor of the main building corridor.

3.4.3 Measurement Cautions

During the measurement campaign, all the doors and windows were closed. Additionally, no humans were allowed to stay between the transmitter and receiver during the measurement operation. There were no other objects in both corridors except small dustbins made of plastic materials, and there exist a few other things already reported in section 3.4.1 (corridor wall and floor materials). The electric lights were switched off in the measuring area to eliminate any possible light impacts on the propagating electromagnetic wave.

3.4.4 Description of the Measurement Campaigns

The first measurement operations were conducted in the corridor of the IT convergence building [Figs. 3.7(a), and 3.7(b)]. The Tx was installed 5 m from the back wall (along the longitudinal direction) and in the center of the hallway, using a guided horn antenna. The antennas for different frequency experiments were changed where the antenna gains were 10, 20, and 20 dBi for the 3.7 GHz directional antenna, 28 GHz directional antenna, 28 GHz TAS antenna, respectively, as mentioned earlier. The trial data were

collected at every 10 m distance of the IT convergence corridor (Fig. 3.5), and 14, 20, 30, 40, 50, 60, 70, 80, 90, 100, 120, 140, 160, 180, 200, 220, 240, and 260 m of the main building corridor (Fig. 3.6). Following the procedure, 9 LOS experimental results at very 3.7, 28, and 28 GHz (TAS) frequencies at the IT convergence corridor and 18 measurement results at every 3.7 and 28 GHz frequency in the main building corridor, were collected.

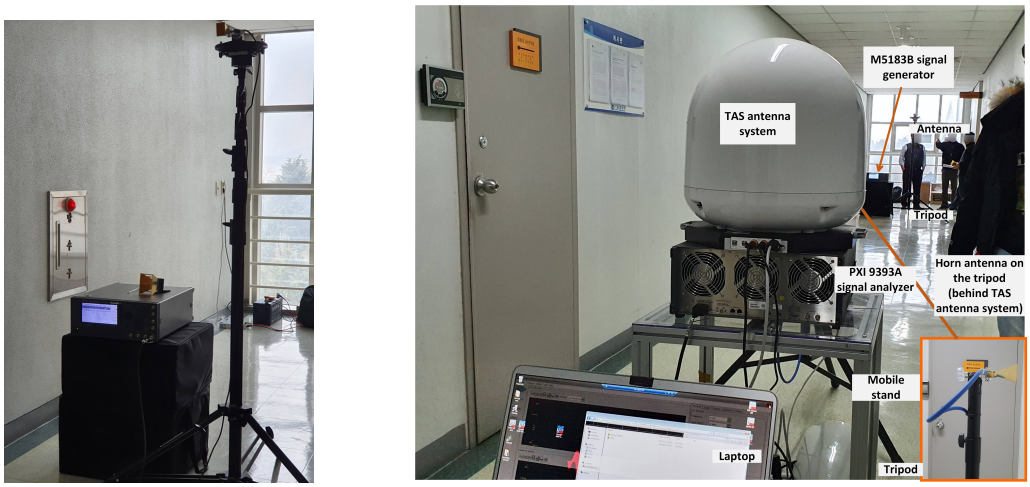

(a) (b)

Figure 3.7: (a) Location of the transmitter at the corridor of the IT convergence building on the 10^{th} floor. (b) A snapshot of the moving facility of the receiver at the IT convergence building on the 10^{th} floor.

The second campaign was operated in the main building of CU [see Fig. 3.8(a), 3.8(b)] which has been recorded as the most extended building in the 'Guinness book of records' some years ago [121]. The same procedure of IT corridor measurement is followed to assess the path loss in the corridor as in the IT convergence building, except the TAS receiver data were not measured. The layout of the main building corridor is given in Fig. 3.6.

(a)

(b)

Figure 3.8: (a) Vacant corridor on the 3rd floor of the main building just before the measurement campaign. (b) A snapshot of the measurement setup of the main building.

3.5 Measurements in the Indoor Tunnel

This section describes the measuring technique, soundings, and instruments used for the campaign and channel sounder.

3.5.1 Measurement Equipment

The measurement equipment used for tunnel path loss measurement is already reported in section 3.3. All these settings are applicable for the tunnel measurement campaign, and the additional parameter transmitter and receiver height are given in Table 3.4. The description of the signal generator and signal analyzer is the same as explained in sections 3.3.1 and 3.3.2, respectively.

Table 3.4: Transmitter and receiver antenna heights in tunnel.

Parameters	3 GHz	28 GHz	28 GHz TAS
Tx antenna height (m)	2	2	2
Rx antenna height (m)	1.5	1.5	1.5

Figure 3.9: Bird's eye view of campaigned propagation measurement at train tunnel.

3.5.2 Campaigned Description

The measurement campaign site is Mangyang tunnel 2, located at Mangyangri, Giseongmyeon, Uljin-gun, Gyeongsangbuk-do, South Korea. The newly built 'Mangyang tunnel 2' will be used for train transportation. The campaign was done before its opening for train transportation; consequently, the safety issue was easily ensured. TA Engineering Inc, South Korea, provided all equipment and technical support in the measurement campaign. The organization can deploy a physical transmitter and receiver, a mobile

(a)

(b)

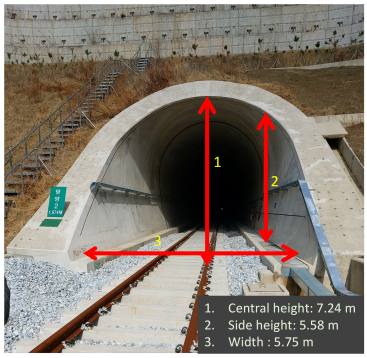

(c)

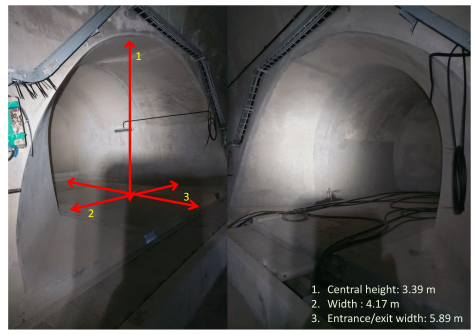

(d)

Figure 3.10: (a) Receiver movement trolley on the train rail, (b) Transmitter and the receiver together in an initial measurement, (c) Tunnel geometry in the entrance of one side, and (d) Typical shape irregularities inside the tunnel.

trolley, and other experimental facilities. Mechanical adjustments allow the transmitter's antenna and material to be modified. Figs. 3.9 and 3.10, respectively, show the tunnel measurement site's bird's eye view and snapshots of the measurement campaigns. The receiver unit was installed on a specially designed trolley for experimental purposes. The transmitter's horn antenna was directed towards the central receiver unit where the receiver trolley was moved inside the tunnel, at regular intervals of 10 m up to 1500 m and then

in the rest of the path at a regular interval of 20 m, the received signal strength was measured. In that way, the received signal was measured in 160 places.

3.6 Data Pre-processing

Path loss is crucial for radio channel models to design wireless networks' link budget and coverage. The path loss of a radio link can be calculated by Equation (3.3):

$$PL = P_{Tx} - P_{Rx} + G_{Tx} + G_{Rx} - C_{Tx} - C_{Rx} \tag{3.3}$$

where P_{Tx} is the transmitted signal power, P_{Rx} is the received signal power, G_{Tx} and G_{Rx} are the gains of the used antennas, and C_{Tx}, C_{Rx} are the cable loss at the Tx and Rx sides, respectively. The received power was measured, and the other gain-related parameters from the system specification and the datasheets.

4. Proposed Path Loss Model for Outdoor and Indoor Links

Rainfall is the significant propagation impairment at millimeter-wave bands at outdoor links, which must be considered during the link budget planning. In this study, the rain attenuation results obtained from experimental data, existing models: ITU-R 530.17, Lin, and Revised Silva Mello (RSM), and proposed Supervised Artificial Neural Network (SANN) at K, Ka, and E-bands for terrestrial links in South Korea, were investigated (section 4.1). Besides, using the previously known links, attenuation-based path loss due to rain can be benefited for quick monitoring of rain attenuation in a particular channel. Consequently, a rain-derived path loss model for frequency and polarization was derived in section 4.2.

4.1 Proposed SANN-based Technique of Path loss due to Rain at Outdoor Terrestrial Links

In this study, a SANN with five input layers equal to the dimension of the feature elements, such as rain rate, raindrop, frequency, polarization, link distance, and a single hidden layer consisting of nine neurons one output layer was implemented. The dimension of hidden neurons is obtained from the general principle, where the number of hidden nodes is less than twice the number of input layers [122, 123].

Bayes' rule provides the model output y conditioned on the input x_i as

the joint probability density distribution $f(x_i, y)$ divided by the marginal $f(x_i)$, i.e., to predict the output observation y given the training input x_i. Therefore, applying conditional probability distribution function $f(y/x_i)$ in predicting the target RSL given training inputs can be written as Equation (4.1) [124].

$$f(y/x_i) = \sum_{n=1}^{n} \frac{f(x_i, y)}{f(x_i)} = \sum_{n=1}^{n} \frac{f(x_i/y)f(y)}{f(x_i)} \tag{4.1}$$

where $f(y/x_i)$, $f(x)$, and $f(y)$ represent the probability distribution functions of predicted output, input, and target y, respectively, whereas $f(x_i/y)$ depicts the conditional probability distribution function of input x_i. Assuming the input x_i follows Gaussian distribution, the probability density function is given by Equation (4.2) [125]:

$$f(x_i/y) = \frac{1}{(2\pi)^{n/2}(C^{1/2})} e^{(\frac{1}{2}[(x-m_{xi}).C^{-1}.(x-m_{xi})^T])} \tag{4.2}$$

where C and m_{xi} are the co-variance and mean of the normal distribution, respectively.

An ANN is a function α_j of the input $x = (x_1, x_2, x_3, \ldots, x_L)$ weighted by a vector of weights $\omega = (\omega_{j1}, \omega_{j2}, \omega_{j3}, \ldots, \omega_{jL})$ plus a neuron bias β_j, and is related to an activation function α. For a network with N layers, the forward propagation of the SANN maps the input vectors x_i to the target output y through the hidden layer, which introduces several neurons and an activation function for each neuron as given by Equations (4.3)~(4.4) [126, 127].

$$Z^{[n]} = \omega^{[n]T} \alpha^{[n-1]} + \beta^{[n]}, 1 \leq n \leq N \tag{4.3}$$

$$\alpha^{[0]} = x_i \tag{4.4}$$

ANN models can apply nonlinear activation functions to produce very distributed representations. The activation function $\alpha^{[n]}$ can have many functional forms. In this work, the sigmoid function was considered as in Equation (4.5):

$$\alpha^{[n]} = \frac{1}{1+exp(-Z^{[n]})}, 1 \leq n \leq N \tag{4.5}$$

where N, $\alpha^{[n]}$, and $z^{[n]}$ indicate the total number of layers, activation function, and transformation on the n^{th} layer, respectively, and the parameters of the transformation are defined as $\omega^{[n]}$ and $\beta^{[n]}$ for layer n.

Backpropagation reduces the error between the prediction and the actual value. Backward propagation occurs from output y to input x_i through the neural network. Backpropagation computes the gradient in the weight space of a forward propagation neural network concerning a loss function. A loss function $L(y, \alpha)$ is adopted to measure the discrepancy between the target output y and computed output α. For regression analysis problems, the squared error can be used as a loss function, as given by Equation (4.6) [128]:

$$L(y, \alpha) = \frac{1}{2m} \sum_{m=1}^{m} (|y - \alpha|^2) \tag{4.6}$$

There are three layers (N) specific to this paper, including the input, hidden, and output layers. The input, hidden, and output layers are represented by '0,' '1,' and '2,' respectively. The number of units in the input, hidden, and output layers are 5, 9, and 1, respectively. The dataset was divided into

80% and 20% for training and validation of the proposed model, respectively. The dataset contains 5×162720 sample-input features and 162720 samples target of the received signal level. Five input features, including rainfall rate, raindrop size, frequency, polarization, and link distance, as well as nine nodes in the hidden layer, were adopted. Therefore, the weight matrices of layer 1 or hidden layer are (9, 5), the bias $\beta^{[1]}$, transformer $z^{[1]}$ and the output of hidden layer $\alpha^{[1]}$ vectors are (9, 1), whereas $z^{[2]}$ and the final output $\alpha^{[2]}$ are (1, 1) vectors as expressed in Equations (4.7), (4.8), (4.9), and (4.10):

$$\begin{bmatrix} z_1^{[1]} \\ z_2^{[1]} \\ \vdots \\ z_9^{[1]} \end{bmatrix} = \begin{pmatrix} \omega_{1,1}^{[1]} & \omega_{1,2}^{[1]} & \cdots & \omega_{1,5}^{[1]} \\ \omega_{2,1}^{[1]} & \omega_{2,2}^{[1]} & \cdots & \omega_{2,5}^{[1]} \\ \vdots & \vdots & \ddots & \vdots \\ \omega_{9,1}^{[1]} & \omega_{9,2}^{[1]} & \cdots & \omega_{9,5}^{[1]} \end{pmatrix} \begin{bmatrix} x_1 \\ x_2 \\ \vdots \\ x_5 \end{bmatrix} + \begin{bmatrix} \beta_1^{[1]} \\ \beta_2^{[1]} \\ \vdots \\ \beta_9^{[1]} \end{bmatrix} \tag{4.7}$$

$$\alpha^{[1]} = \begin{bmatrix} \alpha_1^{[1]} \\ \alpha_2^{[1]} \\ \vdots \\ \alpha_9^{[1]} \end{bmatrix} \tag{4.8}$$

$$\begin{bmatrix} z^{[2]} \end{bmatrix} = \begin{bmatrix} \omega_{1,1}^{[2]} & \omega_{1,2}^{[2]} & \omega_{1,9}^{[2]} \end{bmatrix} \begin{bmatrix} \alpha_1^{[1]} \\ \alpha_2^{[1]} \\ \vdots \\ \alpha_9^{[1]} \end{bmatrix} + \begin{bmatrix} \beta^{[2]} \end{bmatrix} \tag{4.9}$$

$$\alpha^{[2]} = \frac{1}{1 + exp(-Z^{[2]})} \tag{4.10}$$

where $\omega_{jn}^{[1]}$ and $\omega_{jn}^{[2]}$ denote the weight matrices of the hidden and output lay-

ers, respectively, while $\beta_j^{[1]}$ and $\beta_j^{[2]}$ represent the bias vectors of the hidden and output layers, respectively. The vector $Z_j^{[1]}$ represents the input to the output layer, whereas $Z_j^{[2]}$ provides the output of the forward propagation.

Once the input has been transmitted to the output via forward propagation, the following steps involve comparing the predicted output with the target and evaluating the error and fine-tuning parameters such as weight and bias for optimal performance. Meanwhile, the cost function does not relate to the network's weights and bias; hence, defining a sensitivity measure for informing the changes and transmitting to the input via backward propagation [129]. A stochastic gradient descent function is employed to update the bias and weights of the output layer, as expressed in the Equations (4.11), and (4.12):

$$\omega^{[n]} = \omega^{[l]} - \gamma d\omega^{[n]}, 1 \leq n \leq N \tag{4.11}$$

$$\beta^{[n]} = \beta^{[n]} - \gamma d\beta^{[n]}, 1 \leq n \leq N \tag{4.12}$$

where γ represents the learning rate concerning the output layer.

The loss function's derivative determines the value's sensitivity to change in response to a change in its input value. Furthermore, the gradient indicates the extent to which the input parameter needs to change to minimize the loss function, as expressed in Equations (4.13), (4.14),(4.15), and (4.16):

$$dZ^{[n]} = \frac{\partial L(y, \alpha^{[n]})}{\partial z^{[n]})} = \alpha^{[n]} - y,\ 1 \leq n \leq N \tag{4.13}$$

$$d\omega^{[N]} = \frac{\partial L(y, \alpha^{[N]})}{\partial z^{[n]})} \frac{\partial z^{[n]})}{\partial \omega^{[n]})} = dZ^{[n]} \alpha^{[n]T},\ 1 \leq n \leq N \tag{4.14}$$

$$d\beta^{[n]} = \frac{1}{m} dZ^{[n]},\ 1 \leq n \leq N \tag{4.15}$$

$$dz^{[n-1]} = d\omega^{[n]T} dZ^{[n]} g^{[n]}({}^{[n]}),\ 1 \leq n \leq N \tag{4.16}$$

4.2 Proposed Rain-derived Path Loss Characterization using base Frequency and Polarization

In this study, a new prediction technique by applying a Supervised Artificial Neural Network (SANN) based on the measured attenuation data at two different frequencies of the same rain events were proposed. The neural network considered here is straightforward: single input, single hidden, and single output layer. The data were divided into 80% and 20% for the training and testing of our proposed model, respectively. The dataset contains 162,720 input features and 162,720 targets of the received signal level for terrestrial and slant links.

An ANN is a function of the input $x = (x_1, x_2, \ldots, x_L)$ weighted by a vector of weights $\omega = \omega_1, \omega_2, \ldots, \omega_L$ plus a neuron bias β, and is related to an activation function a_p. For an N-layer network, the forward ANN propagation of an x_L vector, which introduces several neurons and an activation function for each neuron, is mapped into the target output y for each layer as given by Equation (4.17).

$$y = \omega^T x_i + \beta \tag{4.17}$$

ANNs use the active feature in the hidden layer to perform complex calculations and then move the result to the output layer. In this study, the sigmoid function was considered as given by Equation (4.18):

$$a_p = \frac{1}{1+e^{-y}} \tag{4.18}$$

where y and a_p represent the transformation and activation functions of the layer, respectively, and w and $\beta^{[n]}$ represents the transformation parameters for the layer.

Equation (4.18), shows that the backward distribution occurs from output a_p to input x_i through the neural network. Backpropagation was used to reduce the estimated and real measured attenuation error. Backpropagation measures the gradient proportional to the loss function in the weight space of a forward-distributed neural network. $L(a_p, a_m)$ is used to calculate the disparity between the target output a_m and computed output a_p. For regression analysis problems, a squared error can be used as a loss function is given by Equation (4.19) [128]:

$$L(a_p, a_m) = \frac{1}{2N}\left[\sum_{i=1}^{N}(a_{p_i} - a_{m_i})^2\right] \tag{4.19}$$

The next stage in optimizing efficiency is comparing the predicted output with the target and identifying the error and acceptable adjustment factors, such as weight and biases. After forward propagation of the input to the output, it will be necessary to compare the expected output with the goal,

evaluate the error, and adjust parameters, such as weight and biases, to yield optimal results. The cost function does not explicitly correlate network weights and bias; hence, a sensitivity measure must be identified to notify the changes and transmit them back to the input [129]. A stochastic gradient descent function is utilized in the following Equations (4.20) and (4.21) to change the biases and weights of the output layer:

$$\omega+ = \omega - r \cdot \partial\omega \tag{4.20}$$

$$\beta+ = \beta - r \cdot \partial\beta \tag{4.21}$$

where r represents the learning rate with respect to the output layer. The loss function derivative measures the sensitivity of the changes in the loss function value as its input value changes. The gradient denotes the input parameter that needs to be modified to minimize the loss function, as expressed below:

$$\partial y = \frac{\partial L(a_p, a_m)}{\partial y} = a_p - a_m \tag{4.22}$$

$$\partial\omega = \partial y \cdot a_p \tag{4.23}$$

$$\partial\beta = \frac{1}{n}\partial y \tag{4.24}$$

The $d\omega$ and $d\beta$ values are computed to update ω and β, as shown in Equations (4.23) and (4.24), respectively. As a result, the weights and the

biases are updated in Equations (4.20) and (4.21), respectively. The same neural network was used to calculate four types of scaling: 18 GHz to 38 GHz, 12 GHz to 20 GHz, 18 GHz (HP) to 18 GHz (VP), and 18 GHz (VP) to 18 GHz (HP), where the training datasets were according to Table 4.1.

Table 4.1: Dataset descriptions of the predicted model.

Link	Conversion	Input data	Target data	Scaling
terrestrial	18 GHz to 38 GHz	attenuation at 18 GHz	attenuation at 38 GHz	frequency
slant	12 GHz to 20 GHz	attenuation at 12 GHz	attenuation at 20 GHz	frequency
terrestrial	HP to VP at 18 GHz	attenuation at 18 GHz HP	attenuation at 18 GHz VP	polarization
terrestrial	VP to HP at 18 GHz	attenuation at 18 GHz VP	attenuation at 18 GHz HP	polarization

4.3 Optimized Large-scale Model for Indoor Corridor and Tunnel

Absorption and scattering are two primary processes in large-scale signal attenuation. Two models characterize the relationship between path loss and channel distance: single-frequency and multi-frequency models, based on empirical data acquired from channel measurements. The large-scale CI, FI, CIF, and ABG models have a fixed mathematical structure and specific parameters whose values change according to operational frequency, terrain setting, and environmental factors. This section determines the propagation parameters using the CI, FI, CIF, and ABG models, which are discussed in detail in the following sections.

4.3.1 Single Frequency Propagation

CI Model

Equation (4.25) gives the CI model of wave propagation:

$$\mathrm{PL}^{\mathrm{CI}}(f,l) = \mathrm{FSPL}(f,1\text{ m}) + 10n\log_{10}(l) + X_{\sigma}^{\mathrm{CI}}(\mathrm{dB});\ \text{for } l \geq 1\text{ m} \tag{4.25}$$

where $X_{\sigma}^{\mathrm{CI}}(\mu, \sigma^{CI})$ is a Gaussian random variable which is characterized by the standard deviation σ^{CI} is measured in dB and mean value of the random variable is zero ($\mu = 0$). $\mathrm{FSPL}(f,1\text{ m}) = 10\log_{10}(\frac{4\pi f}{c})^2$ is the free space path loss with a referencing distance of 1 m, and n is the Path Loss Exponent (PLE). The CI method presents the large-scale channel fluctuations owing to the shadowing effect [73]. The PLE n path loss pattern is calculated by the MMSE-based optimization method, which matches the data determined to the minimum error (by lowering σ^{CI}) with the actual physical anchor point, representing the freely available space power transmitted by the Tx antenna at the proximity [130].

In Equation (4.25), if $F = \mathrm{PL}^{\mathrm{CI}}(f,d) - \mathrm{FSPL}(f,1\text{ m})$, and $L = 10\log_{10}(d)$, the Minimum Mean Square Error (MMSE)-based optimized parameters can be computed by Equation (4.26):

$$n = \frac{\sum FL}{\sum L^2} \tag{4.26}$$

Thus, the smallest Shadowing Factor (SF) standard variation for the CI model is:

$$\sigma_{min}^{CI} = \sqrt{\frac{\sum(F - nL)^2}{D}} \tag{4.27}$$

where D is the number of the Tx-Rx separation distances or the number of recorded different measurement data.

FI Model

The FI path loss model is given by:

$$\mathrm{PL}^{\mathrm{FI}}(l)[\mathrm{dB}] = \alpha + 10 \cdot \beta \log_{10}(l) + X_{\sigma}^{\mathrm{FI}} \tag{4.28}$$

where α is the floating-intercept in dB and this parameter is equivalent to free space path loss, and β is the slope of the line, which is similar to the PLE, $X_{\sigma}^{\mathrm{FI}}(\mu, \sigma^{FI})$ is the Gaussian random variable with zero mean ($\mu = 0$) and standard deviation σ^{FI}, which defines large-scale signal fluctuations about the mean path loss over the length between the transmitter and receiver. The FI method is used in the Wireless World Initiative New Radio (WINNER) II [131] and 3$^{\mathrm{rd}}$ Generation Partnership Project (3GPP) standards [132]. Remarkably, Equation (4.28) expects two parameters, whereas the CI method only needs a single parameter, PLE parameter n. Comparative analysis between CI and FI path loss methods causes extremely comparable shadow deteriorating default variations in mmwave outdoor channels [57,130,133,134]. The FI path loss model Equation (4.28) uses α as the floating intercept in dB (different from an FSPL reference), and β is the slope of the line (different from a PLE). In Equation (4.28), it was assumed that $G = \mathrm{PL}^{\mathrm{FI}}(d)[\mathrm{dB}]$, and $L = 10\log_{10}(d)$. So, the MMSE-based optimized lowest level SF can be

determined by Equations (4.29), (4.30):

$$\alpha = \frac{\sum L \sum LG - \sum L^2 \sum G}{(\sum L)^2 - D \sum L^2} \tag{4.29}$$

$$\beta = \frac{\sum L \sum G - D \sum LG}{(\sum L)^2 - D \sum L^2} \tag{4.30}$$

The optimum standard deviation of SF can be achieved by replacing α and β in (4.31) with (4.29) and (4.30), respectively. The mean values of all the vector elements are determined directly in the dB scale. Thus, the smallest SF standard variation for the FI model is:

$$\sigma^{\mathrm{FI}} = \sqrt{\sum (G - \alpha - \beta L)^2 / D} \tag{4.31}$$

4.3.2 Multi-frequency Propagation

A multi-frequency method is sufficient since interior spaces exhibit frequency-dependent losses beyond the first meter due to the surrounding environment [55]. This section gives a multi-frequency model called the 'alpha-beta-gamma' model to analyze the experimentally measured attenuation datasets.

CIF Model

In [55], it was considered that a multi-frequency method could be regarded as sufficient in the closed indoor environment as there exists frequency-dependent loss after 1 m distance from the transmitter due to the surrounding environment [55]. The CI model can be customized to implement the

frequency-dependent path loss exponent (CIF) that utilizes the same physically driven free space path loss anchor at 1 m as the CI model. The path loss of the CIF method is given by:

$$PL^{CIF}(f,d)[\text{dB}] = L(f,1m) + \left(n(1-n) + {}^{nbf}/_{f_0}\right) 10 \cdot \log\left({}^{d}/_{1\text{ m}}\right) + S^{\text{CIF}}_{\mu,\sigma} \tag{4.32}$$

where d (m) is the distance between Tx and Rx greater than 1 (m), n is the path loss exponent (PLE) that describes the dependence of propagation loss in the path (in dB) to the logarithm of the distance starting at 1 m, $S^{\text{CIF}}_{\mu,\sigma}$ is the Gaussian random variable with zero mean and standard deviation σ(dB).

This random variable characterizes the large-scale channel fluctuations due to shadowing, and b is the optimization parameter that presents the path loss slope of the linear frequency dependence. $L(1\text{ m})$ is the free-space loss at a distance of 1 m, with f_c being the center frequency $L_0(dB) = 20\log\left({}^{4\pi d_0}/_{\lambda}\right) = 32.4 + 20\log f_c(\text{GHz})$. $f(GHz)$ is the operating carrier frequency and f_0 as the minimum investigated the frequency of operating frequencies [135]. The frequency f_0 is computed as $f_0 = \sum_{k=1}^{K} f_k N_k / \sum_{k=1}^{K} N_k$ where f_0 is the weighted frequency average of all measurements for each particular scene which is determined by adding all over the frequencies, the total number of recorded data N_k at a specific frequency and antenna scenario, multiplied by the corresponding frequency f_k, and dividing that sum by the total number of measurements $\sum_{k=1}^{K} N_k$ taken over all frequencies for that specific scenario and the used transmitter and receiver system. In Equation

(4.32), it was assumed that $F = PL^{CIF}(f,d)[\text{dB}] - L(f,d_0)$, $Z = 10\log(d/d_0)$, $p = n(1-b)$, and $q = nb/f_0$, following MMSE-based optimization, p and q can be computed by Equation (4.33) and (4.34):

$$p = \sum Z^2 f \sum ZFf - \sum Z^2 f^2 \sum ZF / \left(\sum Z^2 f\right)^2 - \sum Z^2 \sum Z^2 f^2 \tag{4.33}$$

$$q = \sum Z^2 f \sum ZF - \sum Z^2 \sum ZFf / \left(\sum Z^2 f\right)^2 - \sum Z^2 \sum Z^2 f^2 \tag{4.34}$$

Equations (4.33)~(4.34), derived the closed-loop solution of the assumed terms p and q. The standard derivation of the shadow factor can be derived by inserting p and q in Equation (4.35). By using the initial definition (assumption) $p = n(1-b)$ and $q = nb/f_0$ the values of n and b can be calculated. Thus, the smallest SF standard variation for the CIF model is:

$$\sigma^{\text{CIF}} = \sqrt{\sum (F - Z(p+qf))^2 / N} \tag{4.35}$$

ABG Model

A three-parameter multi-frequency-type model known as the ABG model has terms depending on frequency and distance to describe the propagation loss at different frequencies [130, 135]. The ABG model equation is given by (4.36):

$$\text{PL}^{\text{ABG}}(f,d)[\text{dB}] = 10\alpha \log_{10}\left(\frac{d}{d_0}\right) + \beta + 10\gamma \log_{10}\left(\frac{f}{1\text{GHz}}\right) + X_\sigma^{\text{ABG}} \tag{4.36}$$

where α and γ are related to path length and frequency component of path

loss of the link, f is the frequency in GHz, and β is a parameter used as an offset tool that lacks any physical importance. The parameter $X_{\sigma}^{\mathrm{ABG}}(\mu, \sigma^{ABG})$ is a Gaussian random variable describing large-scale received signal variations of the mean path loss over the path between the transmitter and receiver. The ABG model might be seen as a multi-frequency expansion of the FI model. It can be shown that if γ =0 or 2 and is deployed for a single frequency, it becomes an FI model. The optimum values of the α, β, and γ coefficients can be determined using the MMSE-based optimization technique. The ABG model can be similar in shape to the CI model if it can be reduced to the CI if α is equal to $20\log(4\pi/c), \beta$ to the PLE n and γ to 2. The ABG model modifies the FI for several frequencies; however, the FI may also be achieved with a single frequency in the ABG model [72]. Since the ABG model needs three parameters, the CI model requires only one parameter, making the CI model more efficient considering the computational complexity. There are critics that the additional two coefficients in the ABG model offer minor enhancement to accuracy [57, 136].

The parameters values obtained through MMSE-based optimization can be determined by assuming $A = \mathrm{PL}^{\mathrm{ABG}}(f, d)[\mathrm{dB}]$, $L = 10\log_{10}(d)$ and $R = 10\log_{10}(f)$ in (4.36), MMSE-based optimized coefficients can be derived, which are shown in Equation (4.37)

$$\alpha\sum L^2 + \beta\sum L + \gamma\sum LR - \sum LA = 0 \tag{4.37a}$$

$$\alpha\sum L + D\beta + \gamma\sum R - \sum A = 0 \tag{4.37b}$$

$$\alpha\sum LR + \beta\sum R + \gamma\sum R^2 - \sum R = 0 \tag{4.37c}$$

The numeric values of α, β, and γ for ABG model can be calculated by solving the matrix (4.38):

$$\begin{pmatrix} \alpha \\ \beta \\ \gamma \end{pmatrix} = \begin{pmatrix} \sum L^2 & \sum L & \sum LR \\ \sum L & D & \sum R \\ \sum LR & \sum R & \sum R^2 \end{pmatrix}^{-1} \begin{pmatrix} \sum LA \\ \sum A \\ \sum RA \end{pmatrix} \tag{4.38}$$

Thus, the SF standard deviation is given by the Equation (4.39):

$$\sigma^{\mathrm{ABG}} = \sqrt{\sum (A - \alpha L - \beta - \gamma R)^2 / D} \tag{4.39}$$

5. Experimental Results

After presenting the proposed techniques to determine path loss in outdoor and indoor microwave links, this chapter contains all results obtained by applying the methods discussed in Chapter 4 with the measured data (as discussed in Chapter 3).

5.1 ANN-based Technique of Path loss due to Rain for Outdoor Terrestrial Links

Rainfall rate data collected by a disdrometer over three years at an integration time of 10 seconds(s) was used to calculate the rain rate distributions with various exceedance time percentages. Using the data obtained from the measured rainfall rate, Fig. 5.1 presents a plot of the CCDF of rainfall rate at a 10-s integration time over a different percentage of exceedance time. The Fig. 5.1 shows that the rain rate ($R_{0.01}$) at 0.01% exceedance time or 99.99% availability is 52 mm/h. This rain rate $R_{0.01}$ value at 0.01% exceedance time is a significant parameter for specific rain attenuation calculation in many models such as ITU-R. For locations where $R_{0.01}$ is unknown, ITU-R P.837-7 [137] can be applied.

The impacts of rainfall on the experimental microwave links are determined from two types of datasets: terrestrial and slant links. In this study – RSL measurements at the receiver during clear air and rainy conditions and rain rate measurements by the disdrometer were used. The information on the rainfall rate allows the prediction of the attenuation induced by rain-

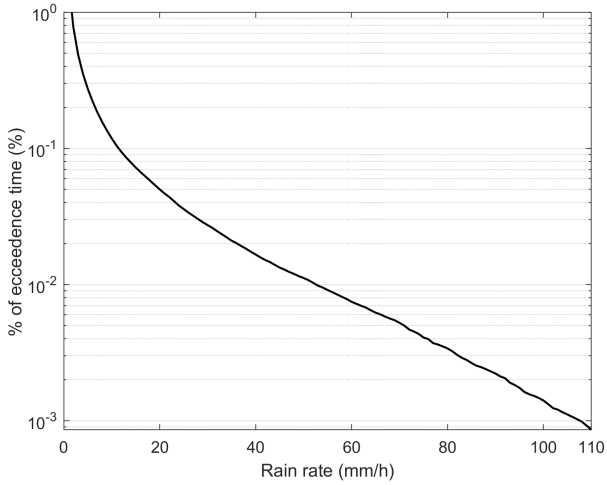

Figure 5.1: Measured rain rate distribution per 10-second integration time for different percentages of exceedance time at Icheon.

fall over the links. The rain attenuation calculated from the received signal power is obtained by determining the difference in RSL between rainy and non-rainy conditions.

Therefore, the rain attenuation CCDF comparison among the measured, existing, and proposed models at various percentages of exceedance time is plotted in Figs. 5.2, 5.3, 5.4, 5.5 for the experimental links operating at 18 GHz horizontal polarization, 18 GHz vertical polarization, 38 GHz vertical polarization, and 75 GHz vertical polarization, respectively. The comparison results are among the measured, different existing rain attenuation prediction models, such as ITU-R P 530–17, RSL Model, Lin, and proposed SANN model. The figures show that SANN agrees well with the measured rain attenuation compared to the three models, especially at 0.1% and 0.01% of exceedance time. It was also observed that the existing rain attenuation

models underestimate the rainfall attenuation, making the network unreliable.

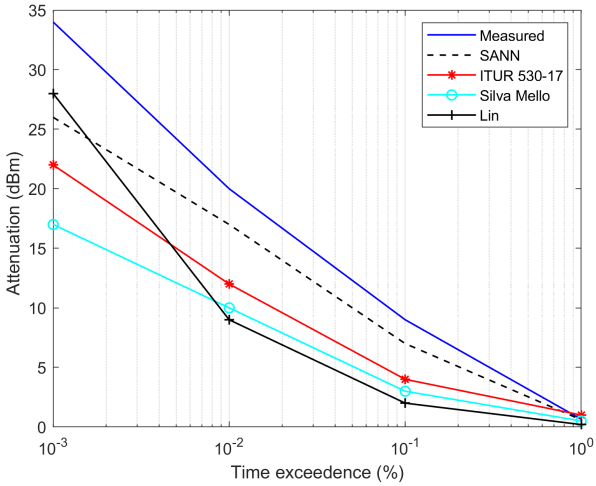

Figure 5.2: Rain attenuation versus time exceedance with 18 GHz horizontal polarization for 3.2 km.

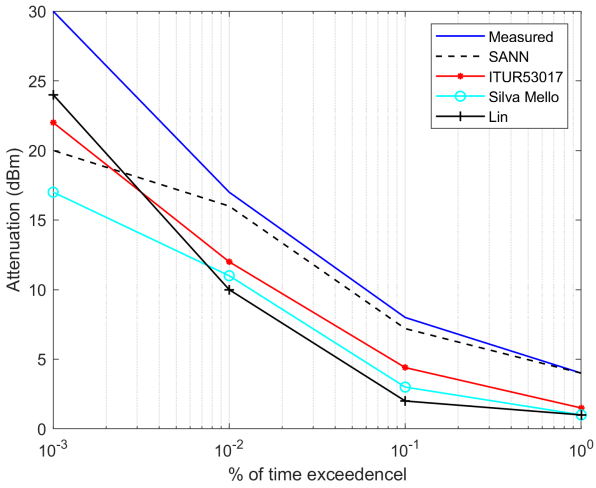

Figure 5.3: Rain attenuation versus time exceedance with 18 GHz vertical polarization for 3.2 km.

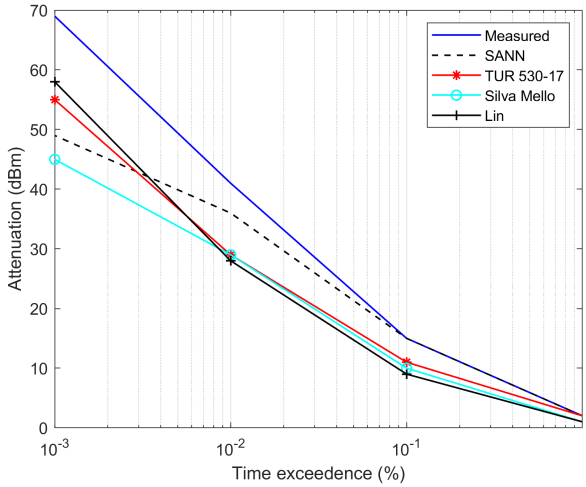

Figure 5.4: Rain attenuation versus time exceedance with 38 GHz vertical polarization for 3.2 km.

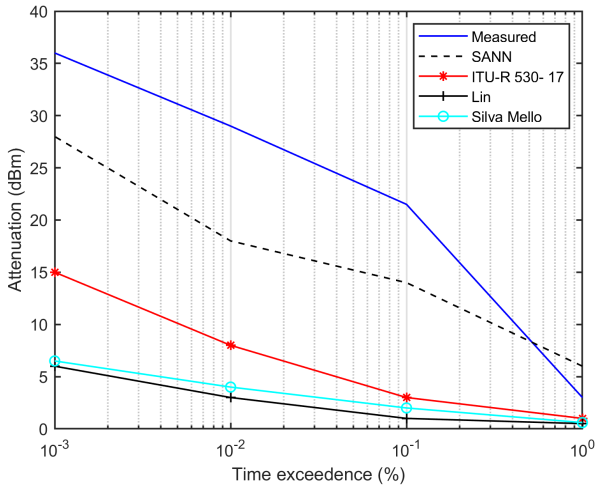

Figure 5.5: Rain attenuation versus time exceedance with 75 GHz vertical polarization for 0.1 km.

Fig. 5.2 and 5.3 show that the horizontal polarization link provides higher rain attenuation than the vertical polarization at the same frequency (18

GHz) and link distance (3.2 km). The horizontal polarization link incurs from higher attenuation because of the nonspherical shape and flattened base of the raindrops; hence, the vertical polarization waves are attenuated less than the horizontal polarization waves. For instance, at 0.01% of the exceedance time, Fig. 5.2, which is horizontally polarized, exhibits 20 dBm attenuation, while Fig. 5.3, the vertically polarized one gives 17 dBm attenuation.

Generally, there is a rapid increase in specific rain fading for frequency bands up to 50 GHz, followed by a more gradual increase from 50 to 100 GHz [138]. This study also agrees that the measured rain attenuation increases as operating frequency shifts from 18 GHz to 38 GHz at the same link distance and polarization, as seen in Fig. 5.3 and 5.4. The rain attenuation at 0.01% of the exceedance time for the 18 GHz vertical polarization presented in Fig. 5.3 is 17 dBm, whereas it is 40 dBm for the 38 GHz vertical polarization shown in Fig. 5.4. Rain attenuation increases as the link distance increases [138]. For instance, at 75 GHz (Fig. 5.5), the measured rain attenuation decreased to 29 dBm, compared to 38 GHz; this is because of the shorter wavelength and link distance (0.1 km) for 75 GHz whereas 3.2 km for 38 GHz.

From these plots, the proposed SANN model agrees well with the measured rain attenuation with various percentages of exceedance times for different frequencies, polarization, and link separations.

Fig. 5.6 shows the CDF distribution against measured rain attenuation at an 18 GHz horizontally polarized and 3.2 km separation link. The maximum CDF is achieved at 20 dBm rain attenuation. The Figure shows that for rain attenuation larger than 20 dBm, in which rainfall rate is greater than 52 mm/h, deep fading is observed at a lower percentage of the year (below 0.01

percentage of time in a year). The Figure indicates that with 99.99 percent availability throughout the year, the attenuation due to rain is less than 20 dBm.

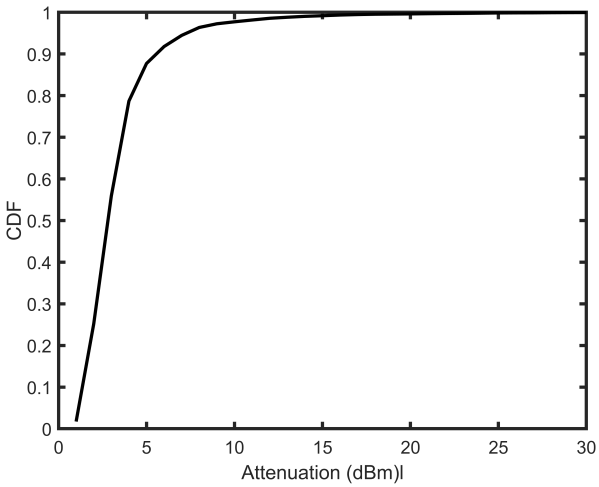

Figure 5.6: Attenuation cumulative distribution for 18 GHz in horizontal polarization.

Fig. 5.7 shows the measured and SANN sample-predicted RSL against rainfall rate at 75 GHz for one-day rain events on the 8^{th} of July 2016. It is observed that as the rainfall rate increases, the corresponding RSL values decrease. The measured- and SANN-predicted Received Signal Levels (RSLs) are well fitted. The Figure shows three rainfall spikes with maximum rain rates of 86 mm/h, 68 mm/h, and 58 mm/h. The corresponding RSL values are -61 dBm, -74.5 dBm, and -70 dBm. Although the first rainfall spike exhibits the highest rainfall rate, its width is narrow, which results in a lower RSL. Therefore, the duration of the rainfall rate also has significant effects.

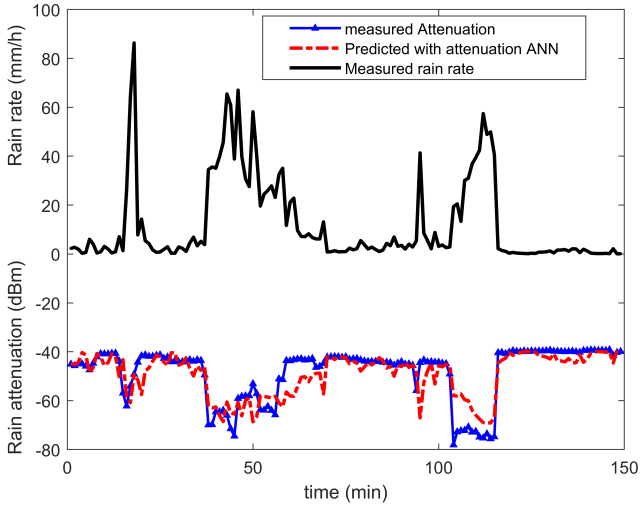

Figure 5.7: Variation of measured and predicted received signal levels concerning the variation of measured rain rate along the path.

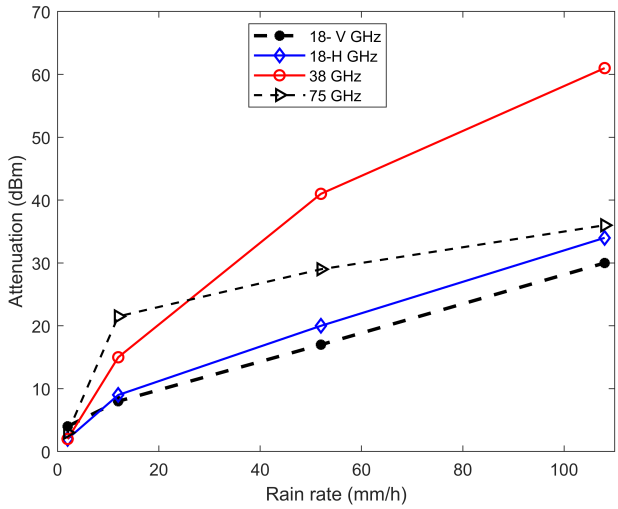

Figure 5.8: Rain attenuation in dBm against rain rate (mm/h).

Fig. 5.8 illustrates the plot of rainfall attenuation versus rain rate for the measurement links of 18 GHz vertical, 18 GHz horizontal, 38 GHz vertical,

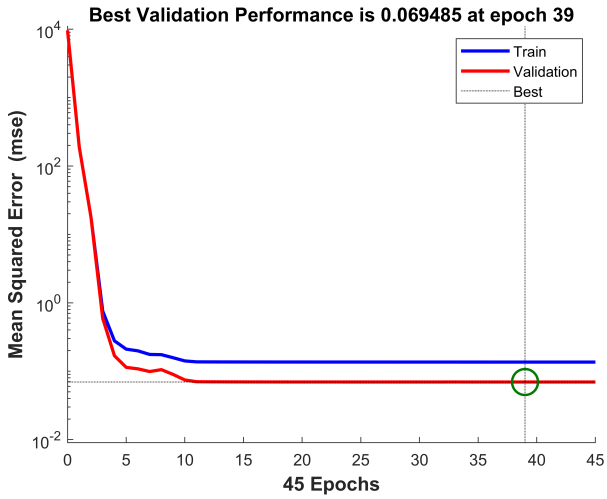

Figure 5.9: MSE plot during training and validation process.

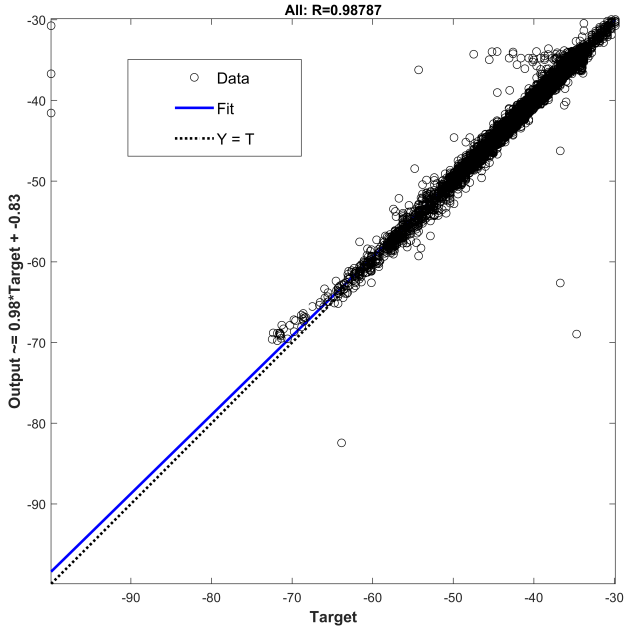

Figure 5.10: Regression plot for 18 GHz horizontal polarization.

and 75 GHz vertical polarized frequency. The Figure depicts the increase in rain attenuation values as the rate of precipitation increases. Fig. 5.8, indicates that lower rainfall rates significantly influence the E-band (75 GHz) spectrum. For rain rates greater than 20 mm/h, the raindrop size is larger than the wavelength of 75 GHz frequency, causing minor scattering problems and resulting in lower attenuation than the 38 GHz frequency [139].

Table 5.1: Relative error probability at 0.01 percentage time exceedance using (5.2).

Models	18 GHz HP	18 GHz VP	38 GHz VP	75 GHz VP
ITU-R 530-17 [19]	-0.4	-0.294	-0.293	-0.724
RSM [33]	-0.5	-0.353	-0.293	-0.8965
Lin [32]	-0.55	-0.411	-0.317	-0.86
SANN [This work]	-0.15	-0.0588	-0.122	-0.38

The 'goodness of fit' function was considered, which, in general, measures how well the observed data correspond to the fitted (assumed) model. The 'goodness of fit' function can be defined by Equation (5.1).

$$\epsilon(P)_T = \frac{A_{\%p,\,p} - A_{\%p,\,m}}{A_{\%p,\,m}} \times 100[\%] \tag{5.1}$$

where $\epsilon(P)_{\mathrm{T}}$, $A_{\%p,m}$, and $A_{\%p,p}$represent the predicted error of the rain attenuation model, measured attenuation in dBm, and predicted attenuation in dBm, respectively.

Fig. 5.9 presents the performance goal of SANN training for the 18 GHz vertical polarization link, which exhibits the best performance with a Mean Squared Error (MSE) of 0.112. Similarly, the MSE values for the 18- GHz

horizontal, 38 GHz, and 75 GHz bands are 0.134, 3.85, and 4.62, respectively. Fig. 5.10 shows the regression plot (R^2) of the 9.985 regression coefficient for the 18 GHz vertical polarization band. Similarly, the regression coefficients for the 18 GHz horizontal, 38 GHz, and 75 GHz bands are 9.98, 9.95, and 9.58, respectively. In general, the regression values of R^2 greater than 0.9 exhibits a good fit between the model output and corresponding target, as shown in Fig. 5.10.

Mathematically, the regression R^2, which indicate the determination coefficient between the predicted and actual outputs, is defined by equation (5.2):

$$R^2 = \frac{\text{Explained variation}}{\text{Total variation}} \tag{5.2}$$

The calculated relative error probability at 0.01% of the time for the 18 GHz with vertical and horizontal polarizations, 38 GHz, and 75 GHz with vertical polarization for each model is presented in Table 5.1. It is observed that almost all prediction models underestimate the measured cumulative rain attenuation statistics in South Korea.

5.2 Rain-derived Path Loss Characterization using base Parameters

This study considers the measured RSL data at low and high operating frequencies for frequency scaling and two types of polarization for polarization scaling. Rain attenuation, determined by the obtained RSL, was accomplished by determining the RSL difference between rainy and non-rainy

times. Knowledge of the precipitation levels provides a rain attenuation prediction over the links.

As a result, the rain attenuation CCDF relation between the measured, scaled from the existing model, and the proposed models at different exceedance time percentages are plotted in Figs. 5.11, 5.12, 5.13, and 5.14. Figs. 5.11 and 5.12 present the frequency scaling for terrestrial and satellite links, respectively. Figs. 5.13 and 5.14 correspond to polarization scaling. A detailed description of these Figs. is provided below:

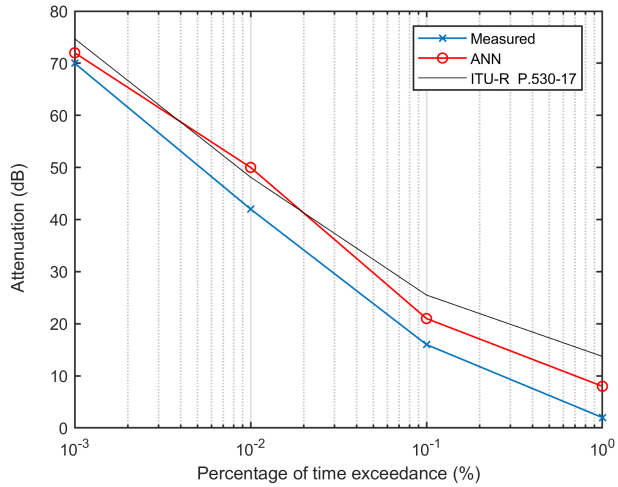

Figure 5.11: Predicted attenuation at 38 GHz using ANN and ITU-R frequency scaling technique from 18 GHz (terrestrial link).

Fig. 5.11 shows the measured attenuation versus the time exceedance percentage of the experimental terrestrial link using frequency scaling. Here, the measured attenuation means the attenuation obtained from the recorded RSL for the 38 GHz radio link. The red line marked by the small circle represents the predicted attenuation generated through the ANN network

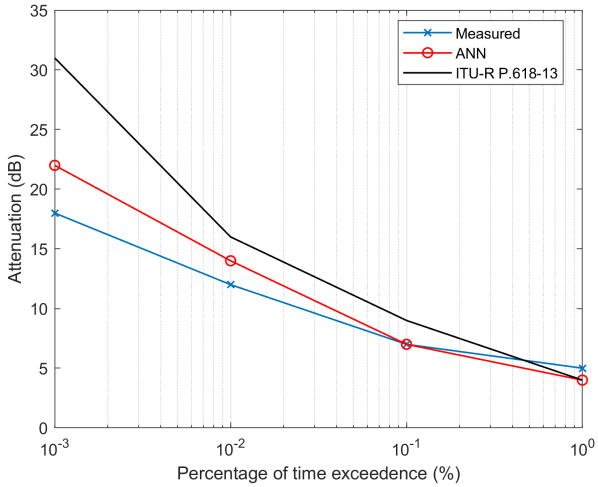

Figure 5.12: Predicted attenuation at 20 GHz using ANN and ITU-R frequency scaling techniques [42] from 12 GHz (slant link).

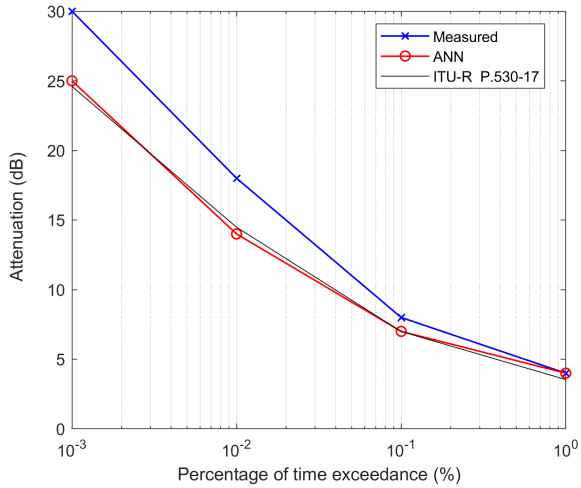

Figure 5.13: Predicted attenuation at 18 GHz vertical polarization from 18 GHz horizontal polarization using ANN and ITU-R polarization scaling techniques [19] from the measured terrestrial link.

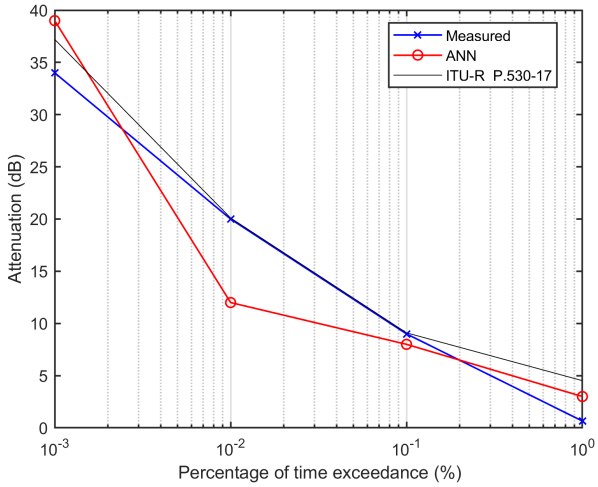

Figure 5.14: Predicted attenuation at 18 GHz horizontal polarization from 18 GHz vertical polarization using ANN and ITU-R polarization scaling techniques [19] from the measured terrestrial link.

taking attenuation at 18 GHz as input and attenuation at 38 GHz as a target. In the same Figure, the black line represents the attenuation obtained by scaling from 18 GHz to 38 GHz using the existing ITU-R P.530-17 formula. As shown in Fig. 5.11, the overall attenuation predicted by the ANN model is well-matched to the measurement compared to the value predicted by the ITU-R P.530-17 scaled formula.

Fig. 5.12 shows the frequency scaling plot from 12 GHz to 20 GHz frequency for satellite links, and the description of this Figure is almost the same as that in Fig. 5.11, except for the slant link case application. The Figure shows that the predicted attenuation through the ANN is closer to the measured result compared to the ITU-R scaled attenuation. Overall, the ANN model also showed good performance in predicting the attenuation of the slant link.

Fig. 5.13 depicts the performance of polarization scaling of rain attenuation comparison among measured, scaled through the ANN model, and scaled using the ITU-R model [19] at 18 GHz over the terrestrial link. The scaling was undertaken from the 18 GHz horizontal to the 18 GHz vertical polarization. Here, the ITU-R-generated attenuation was less compared to the measured attenuation. Considering the four points, the proposed ANN model showed better performance at two points than the ITU-R model, while for one point, ANN and ITU-R are the same, and for one point, ANN did not show better performance than the ITU-R model. Therefore, the overall performance is satisfactory compared to the ITU-R P.530-17 scaled model.

Fig. 5.14 shows the reverse prediction technique compared to Fig. 5.13, where the predicted attenuation is plotted for an 18 GHz horizontal link from the 18 GHz vertically polarized measured rain attenuation datasets; at this point, the performance of the proposed ANN model is not satisfactory. On the other hand, the ITU-R model comparatively shows better prediction capability as the predicted attenuation matches the measured attenuation for most of the rain attenuation time exceedance.

5.3 Optimized Large-scale Path Loss Models for Indoor Corridors

Path loss measuring at 3.7 and 28 GHz were conducted to examine the university campus's long-term path loss models coefficients. As explained earlier, in LOS conditions, that received signal strength was measured with sophisticated devices. The following long-term path loss models: FI, CI, CIF, and ABG were used in this work. Three different environments have

been examined at two frequencies, 3.7 and 28 GHz. The measurement drive was carried out in a 100-meter-long hallway, in the first case in Horizontal-Horizontal polarization (H-H) co-polarization and the second on the same floor, but the receiver was totally inside the closed computer lab. Table 5.2 and 5.3 show the coefficients of the FI, CI, CIF, and ABG models and standard deviation (σ) values, respectively.

Table 5.2: Coefficients of different propagation techniques for the indoor corridor.

Loc.	Fre.GHz	CI	FI:α	CIF	ABG:β	CI:n	FI:β	CIF:n	ABG:α	CIF:b	ABG:γ
IT	3.7	43.8	46.5	43.8	29.5	1.8	1.7	1.7	1.4	0.1	5.6
	28	61.4	58.7	61.4	29.5	1.8	1.9	1.7	1.4	0.1	5.6
	28 TAS	61.3	55.6	61.4	29.5	1.8	2.1	1.7	1.4	0.1	5.6
Main	3.7	43.8	54.8	43.8	37.1	1.6	1.1	1.8	1.3	0.1	4.5
	28	61.4	70.6	61.4	37.1	2.1	1.7	1.8	1.3	0.1	4.5

Table 5.3: Shadow factors of CI, CIF, FI, and ABG models obtained for the indoor corridor.

Locat.	Fre. GHz	CI (σ)	FI (σ)	CIF (σ)	ABG(σ)
IT	3.7	1.616	1.541	11.514	9.967
	28	2.936	2.896	3.312	6.893
	28 TAS	4.638	4.520	4.712	7.459
Main	3.7	3.046	2.257	9.100	14.238
	28	4.057	3.679	6.934	14.531

Figs. 5.15~5.18 depicts a logarithmic scale study of measured path loss in the hallway through the CI, CIF, FI, and ABG models at the 3.7 and 28 GHz frequencies. A comparison of the path loss-derived by CI, CIF, FI, and ABG models with the observed results was computed, along with the

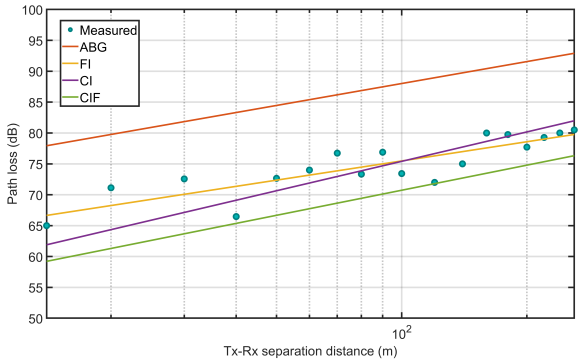

Figure 5.15: CI, FI, CIF, ABG model, and measured path loss in the main building corridor at 3.7 GHz LOS link.

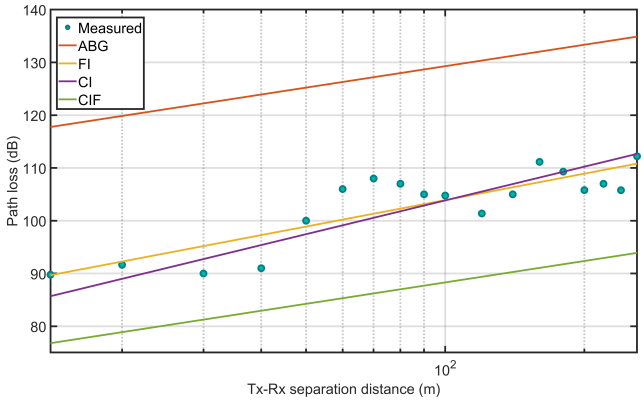

Figure 5.16: CI, FI, CIF, ABG, and measured path loss in the main building corridor at 28 GHz LOS link.

standard deviation. In Fig. 5.15, the measured and the expected attenuation by the CI, CIF, FI, and ABG models was plotted for the measured data at the main building corridor at 3.7 GHz. The figure showed that the CI and FI model fits the path loss attenuation are close to the measured results, whereas the attenuation predicted by the CIF and ABG were not well fitted to the measured data. In Fig. 5.16, the measured and the expected attenu-

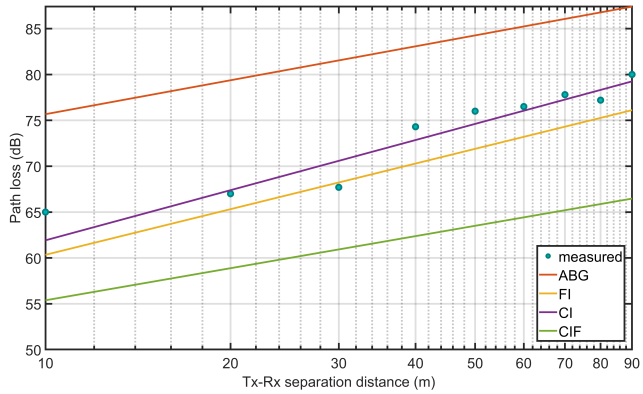

Figure 5.17: CI, FI, CIF, ABG, and measured path loss in the IT convergence building corridor at 3.7 GHz LOS link.

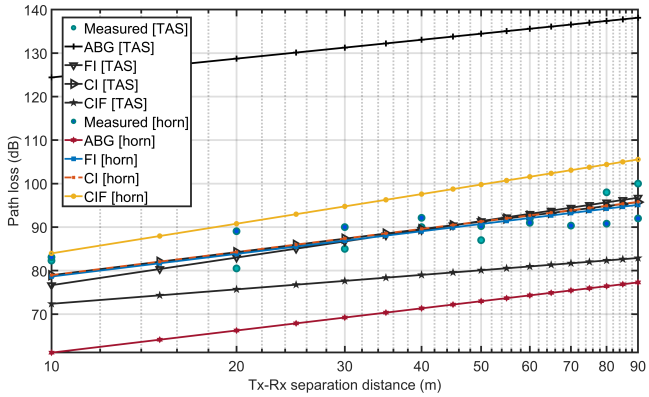

Figure 5.18: CI, FI, CIF, ABG, and measured path loss in the IT convergence building corridor at 28 GHz (TAS) LOS link.

ation by the CI, CIF, FI, and ABG models were plotted for the measured data at the main building corridor at 28 GHz. The figure showed that the CI and FI model fits the path loss attenuation are close to the measured results, whereas the attenuation predicted by the CIF and ABG were not well fitted to the measured data. In Fig. 5.17, the measured and the pre-

dicted attenuation by the CI, CIF, FI, and ABG models was plotted for the measured data at the IT convergence building corridor at 3.7 GHz. The figure showed that the CI and FI model fits the path loss attenuation are close to the measured results, whereas the attenuation predicted by the CIF and ABG were not well fitted to the measured data.

In Fig. 5.18, the measured and the predicted attenuation by the FI, CI, FI, and ABG models were plotted for the IT convergence building corridor measured data at 28 GHz using horn-horn and horn-TAS antenna system respectively in the transmitter and receiver end. The figure showed that the CI and FI model fits the path loss attenuation for both horn-horn and horn-TAS antenna combinations are close to the measured results, whereas the attenuation predicted by the CIF and ABG were not well fitted to the measured data. The standard deviation of the CI model was 3.046, 4.057 in the main building corridor, and 1.616, 2.936, 4.638 respectively, for the frequency of 3.7 GHz (horn), 28 GHz (horn), 28 GHz (TAS). The standard deviation of the CIF model was 9.100, 6.934 in the main building corridor, and 11.514, 3.312 respectively, for the frequency of 3.7 GHz (horn), 28 GHz (horn), 28 GHz (TAS). For the FI model, the standard deviation was 2.257, 3.679 in the main building corridor, and 1.541, 2.896 in the IT convergence building corridor, respectively, for the frequency of 3.7 GHz (horn), 28 GHz (horn), 28 GHz (TAS). For the ABG model, the standard deviation was 14.238, 14.531 in the main building corridor, and 9.967, 6.893 in the IT convergence building corridor, respectively, for the frequency of 3.7 GHz (horn), 28 GHz (horn), 28 GHz (TAS). Fig. 5.19 present the point-to-point standard deviations of the collected data in H-H polarization for several

experiments at frequencies 3.7 and 28 GHz. In the IT building corridor, the P2P fluctuation is 4.5, 4.2, 3.4 dB, respectively, at 3.7, 28, 28 GHz (TAS) frequencies. While in the main building corridor, the P2P fluctuation is 4.2, 6.4 dB, respectively, at 3.7, 28 GHz.

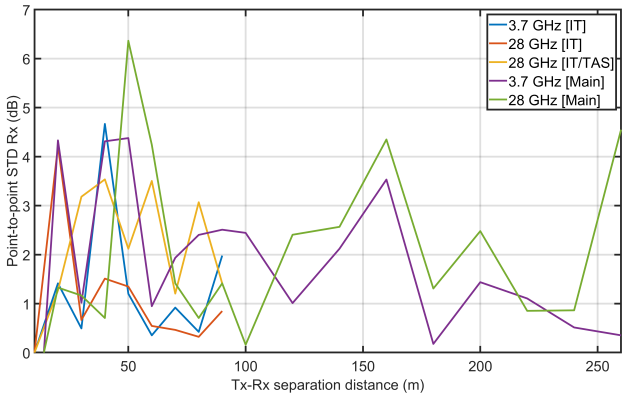

Figure 5.19: Standard deviation of point-to-point power variations in corridors.

5.4 Optimized Large-scale Path Loss Models for Indoor Tunnel

Measurement campaigns at 3.7 and 28 GHz were carried out to examine the parameters of long-term path loss models in a train tunnel. The transmitting antenna was directed towards the inward direction, and the receiver located in the middle of the mobile van was directed towards the receiving antenna. At two frequencies (3.7 and 28 GHz), three different types of channels were created using separate antennas, as mentioned earlier. Table 5.4 shows the coefficients of the CI, FI, CIF, and ABG models.

Fig. 5.20 shows the changes in path loss in the long train tunnel on a semi-log scale. The measured path loss at different points is plotted through

Table 5.4: Coefficients of different of large-scale models for the tunnel.

Fre. GHz	CI	FI:α	CIF	ABG:β	CI:n	FI:β	CIF:n	ABG:α	CIF:b	ABG:γ
3.7	43.81	48.15	43.81	59.41	1.7	1.54	1.61	1.15	-0.07	1.05
28	61.38	82.97	61.38	59.41	1.61	0.85	1.61	1.15	-0.07	1.05
28 TAS	61.38	74.27	61.38	59.41	1.51	1.05	1.61	1.15	-0.07	1.05

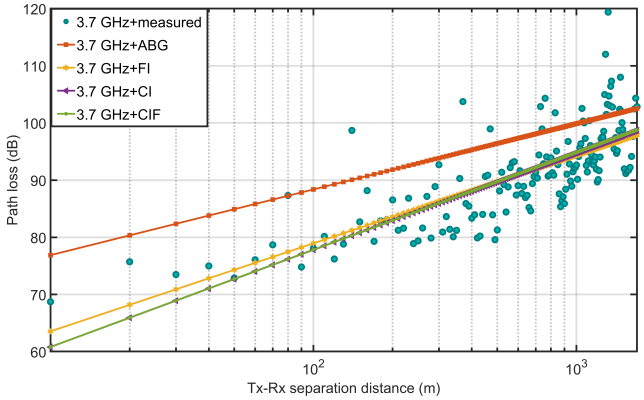

Figure 5.20: CI, FI, CIF, ABG model, and measured path loss in the tunnel at 3.7 GHz.

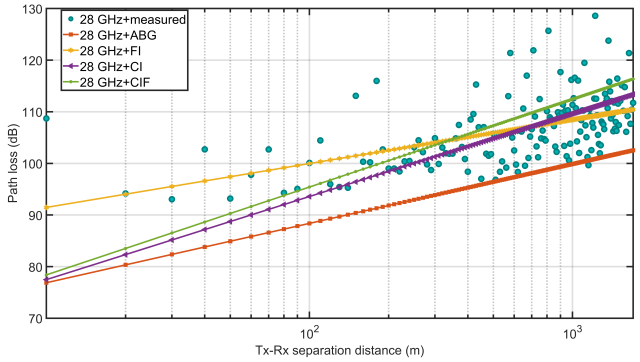

Figure 5.21: CI, FI, CIF, ABG model, and measured path loss in the tunnel at 28 GHz.

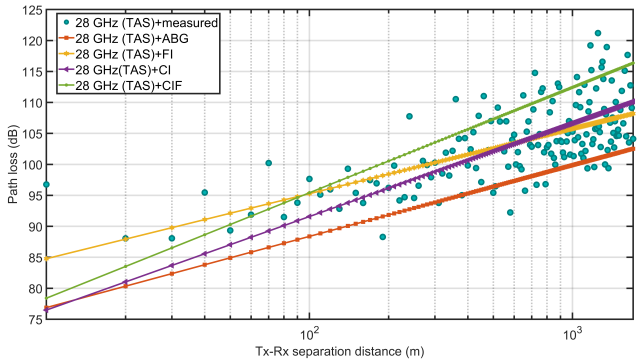

Figure 5.22: CI, FI, CIF, ABG model, and measured path loss in the tunnel at 28 GHz (TAS).

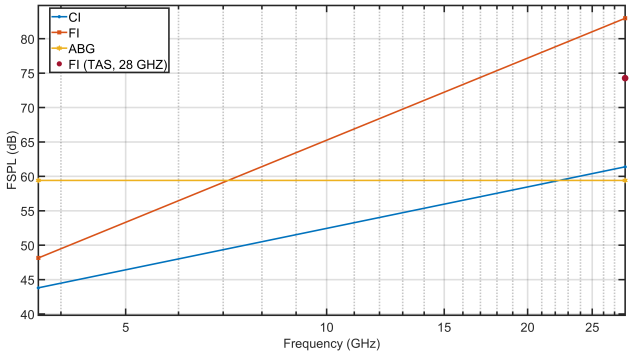

Figure 5.23: FSPL variations at different frequencies developed by CI, FI, CIF, and ABG models.

a scatter plot. The measured path loss was fitted through the CI, FI, CIF, and the ABG model, and all these models are plotted as straight lines. It is noticeable that in Fig. 5.20, the ABG model did not fit well with measured datasets. Except for the ABG model, the other two models, CI, FI, and CIF are competitive considering the prediction performance. Among the CI, FI and CIF show almost identical path loss predictions at the far end side, but there is a variation in near and for FI models compared to the CI and CIF

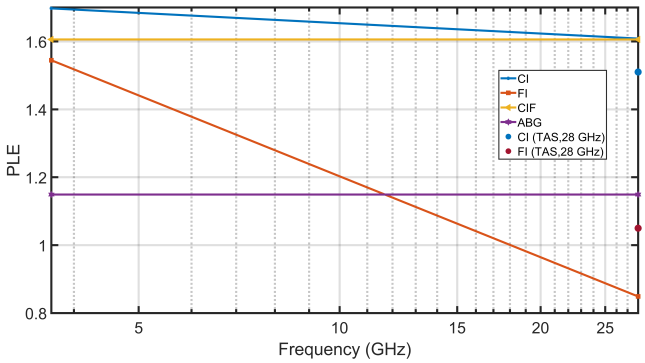

Figure 5.24: PLE variations at different frequencies developed by CI, FI, CIF, and ABG models.

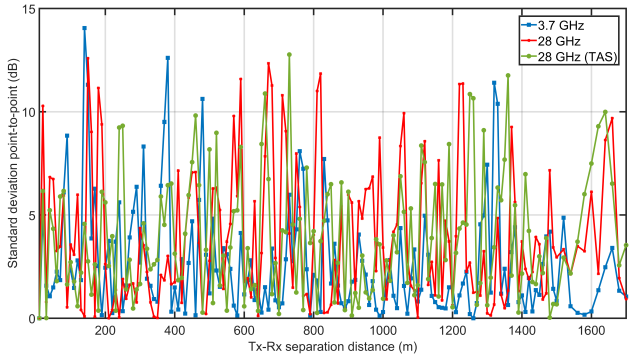

Figure 5.25: Standard deviation of point-to-point variation of received power in the tunnel.

models. The FI model fitted the measured data compared to the CI and CIF models in the near end. Consequently, at 3.7 GHz frequency, the FI model fitted the measured datasets more efficiently compared to the other models.

Fig. 5.21 shows the changes in path loss in the long straight train tunnel in semi-log scale at 28 GHz frequency. Both the CI and the CIF model showed good performance at the far end of the tunnel, but they did not perform well at the near end. At 28 GHz frequency, the ABG model did not

fit well with the measured datasets, whereas the ABG model parameters were calculated through the MMSE-based optimization technique. Among the remaining three models, at 28 GHz, the FI model fitted the measured datasets more efficiently than the CI and CIF models.

Fig. 5.22 shows the changes in path loss in the long straight train tunnel in semi-log scale at 28 GHz frequency. At 28 GHz, the ABG model also did not fit well with the measured datasets with the TAS receiver. The path loss predicted by the FI model fits well with the measured datasets, which is more accurate at the near end and the far end. As shown in Fig. 5.22, FI model performances well at the 28 GHz TAS receiver compared to the CI, CIF, and ABG models.

FSPL Variations in Different Propagation Techniques

Fig. 5.23 shows the changes in FSPL by the CI, FI, CIF, and ABG model. Since the FSPL of the CI and CIF model are the same, the CIF model is not shown here for brevity. The FSPL developed by the ABG model is a constant quantity shown by the straight yellow line marked by a hexagonal-shaped marker. The FSPL of the CI model is much lower than the other models, but it is noticeable in Fig. 5.20, 5.21, 5.22 that the CI model did not outperform the FI model respectively at 3.7, 28, and 28 GHz (TAS) frequencies. The FSPL at 28 GHz with TAS receiver is a different value, as shown here by a single scatter point red dot. Consequently, the FI model has a positive slope of FSPL (even if the single scatter red dot is considered). As a result, the FSPL by the FI model is consistent with the path loss as in Figs. 5.20, 5.21, and 5.22.

PLE Variations at Different Frequencies and Models

Fig. 5.24 shows the changes in PLE for the frequency of FI, CI, CIF, and ABG models. The path loss exponent of the CIF and ABG model is constant over the frequency 3.7 to 28 GHz frequency and 1.6 and 1.1, respectively. The remaining two models, the CI and FI, have a negative slope. For the TAS antenna system in the receiver end, the PLE points show different CI and FI model trends. In the CI model, the PLE created by MMSE optimization is much decreased, but the PLE for the TAS receiver increases in the FI model.

Point to Point Standard Deviation Variations of Received Power

The standard deviation of Point-to-Point (P2P) received power was found as a helpful tool to investigate the variations of the received power in different propagation measurement campaigns as reported in [65, 140]. Fig. 5.25 shows the changes of the measured received power at varying distances in the tunnel at the frequencies of 3.7, 28, and 28 GHz (TAS). A total of 160 points were measured inside the tunnels where at each point, two different frequencies in the S and Ka bands were used where the receiver antenna was horn as TAS, as reported earlier.

Shadow Factor

Shadow fading was calculated as the difference (in dB) between the data points and the trajectory loss anticipated at this distance by Equation (5.3):

$$SF^{(\text{matching })}(d,f)[dB] = PL_{\text{meas.}}\ (d,f) - PL^{(\text{matching })}(d,f) \tag{5.3}$$

The shadow factor follows Gaussian distribution with zero mean ($\mu = 0$) and standard deviation σ, which means the PDF of the SF is given by Equation (5.4):

$$f_X(x) = (1/\sigma\sqrt{2\pi})e^{-x^2/2\sigma^2} \tag{5.4}$$

The histograms were correlated to a Gaussian distribution as predicted; however, the distribution graphs are excluded for brevity. Table 5.5 shows the standard deviation of the CI, FI, CIF, and ABG models.

Table 5.5: Shadow factor of large-scale models for the tunnel.

Fre. GHz	CI(σ)	FI(σ)	CIF(σ)	ABG(σ)
3.7	5.58	5.49	3.91	8.47
28	8.58	5.53	6.53	5.67
28 TAS	10.56	4.86	5.40	7.92

6. Conclusions

In this dissertation, firstly, the measured path loss data due to rain of outdoor microwave links were modeled with proposed ANN-based two models – SANN-based model and another one is ANN-based model where base frequency and polarization link's attenuation datasets are used. Secondly, measured path loss data of indoor corridor and train tunnel were modeled with MMSE-based optimized technique.

6.1 Path Loss due to Rain at Outdoor Links

The results, derived through the SANN-based technique, reveal that existing models underestimate the measured path loss (attenuation). For instance, at 0.01% of exceedance probability, the ITU-R P.530-17, Revised Silva Mello (RSM), Lin, and SANN models underestimated the attenuations by 5 dBm, 6 dBm, 7 dBm, and 1 dBm, respectively, for the 18 GHz vertical polarization. For the 18 GHz horizontal polarization, ITU-R P.530-17, RSM, Lin, and SANN models underestimated the results by 6 dBm, 7 dBm, 8 dBm, and 3 dBm, respectively. For the 38 GHz vertical polarization, although the three models underestimated the results by 11 dBm, SANN underestimated the results by 4 dBm. For the 75 GHz vertical polarization, ITU-R P.530-17, RSM, Lin, and SANN models underestimated the results by 23 dBm, 25 dBm, 26 dBm, and 4 dBm, respectively. At lower rainfall rates (< 30 mm/h), the 75 GHz band exhibits more attenuation, whereas the 38 GHz band experiences more attenuation at a higher rainfall rate.

Although additional experiments are required to validate these conclusions, the results show that the proposed SANN model outperforms the existing models if adequately trained with a sufficient database for the applications of rain-induced attenuation prediction, especially for high-frequency short link-length terrestrial links.

When using the base frequency, the rain-derived path loss technique reveals excellent overall performance for frequency scaling on terrestrial and slant links. The predicted attenuation implications from horizontal to vertical polarization are also good.

6.2 Application of Optimized Large-Scale Models at Indoor Corridors and Tunnel Links

The feasibility of the large-scale path loss models: CI, FI, CIF, and ABG – where the path loss parameters were determined through MMSE-based optimization technique, were investigated for the microwave links at the indoor corridors and tunnel.

According to the results of large-scale models: CI, FI, CIF, and ABG in the indoor corridor, the CI and FI path loss models were identical and matched the measured path loss in two long indoor corridors for LOS horn antenna links. The multi-frequency models CIF and ABG did not show sound performance to fit the measured path loss. The Standard Deviation (STD) of measured path loss was varied highly in the main corridor compared to the IT corridor at 3.7 GHz, but at 28 GHz, such variations were negligible.

CI, FI, CIF, and ABG usage in train tunnels reveals that the ABG model

did not match the observed datasets well across all frequency bands. At 28 GHz, the CI, CIF, and ABG models performed almost identically, but at 3.7 GHz, the FI model more precisely matches the observed data. At 28 GHz frequency, both the antenna type horn and the TAS model produced consistent matching findings with the measured datasets. As a result, the FI model outperformed the other models matching the measured datasets in all measurement situations. Besides, the FI model also showed better performance by yielding a lower standard deviation of the shadow factors. So in every perspective, the FI model provided a more fair propagation loss for the tunnel.

References

1. I. Rodriguez, H. C. Nguyen, N. T. K. Jorgensen, T. B. Sorensen, and P. Mogensen, "Radio propagation into modern buildings: Attenuation measurements in the range from 800 MHz to 18 GHz," in *2014 IEEE 80th Vehicular Technology Conference*. Vancouver, BC, Canada: IEEE, 14~17 Sep. 2014. doi: 10.1109/vtcfall.2014.6966147
2. C. Larsson, F. Harrysson, B.-E. Olsson, and J.-E. Berg, "An outdoor-to-indoor propagation scenario at 28 GHz," in *The 8th European Conference on Antennas and Propagation*. The Hague, Netherlands: IEEE, 6~11 Apr. 2014. doi: 10.1109/eucap.2014.6902534
3. C. A. L. Diakhate, J.-M. Conrat, J.-C. Cousin, and A. Sibille, "Millimeter-wave outdoor-to-indoor channel measurements at 3, 10, 17 and 60 GHz," in *2017 11th European Conference on Antennas and Propagation*. Paris, France: IEEE, 19~24 Mar. 2017. doi: 10.23919/eucap.2017.7928696
4. J. Lee, K.-W. Kim, M.-D. Kim, and J.-J. Park, "Multipath characteristics of Outdoor-to-Indoor propagation based on 32-GHz measurements," in *2020 14th European Conference on Antennas and Propagation (EuCAP)*. Copenhagen, Denmark: IEEE, 15~20 Mar. 2020. doi: 10.23919/eucap48036.2020.9135828
5. White paper on, "5G channel model for bands up to 100 GHz," in *Global Communications Conference, 3rd Workshop on Mobile Communications in Higher Frequency Bands*, Washington DC, U.S.A, 2016. [Online]. Available: http://www.5gworkshops.com/5GCM.html (accessed on 14 Jan. 2022)
6. S. Deng, G. R. MacCartney, and T. S. Rappaport, "Indoor and outdoor 5G diffraction measurements and models at 10, 20, and 26 GHz," in *2016 IEEE Global Communications Conference*. Washington, DC, USA: IEEE, 4~8 Dec. 2016. doi: 10.1109/glocom.2016.7841898
7. D. E. Boubiche, A.-S. K. Pathan, J. Lloret, H. Zhou, S. Hong, S. O. Amin, and M. A. Feki, "Advanced industrial wireless sensor networks and intelligent IoT," *IEEE Communications Magazine*, vol. 56, no. 2, pp. 14~15, Feb. 2018. doi: 10.1109/mcom.2018.8291108

8. F. A. Semire, R. Mohd-Mokhtar, and I. A. Akanbi, "Validation of new ITU-R rain attenuation prediction model over malaysia equatorial region," *MAPAN*, vol. 34, no. 1, pp. 71~77, Nov. 2018. doi: 10.1007/s12647-018-0295-z
9. L. Luini, G. Roveda, M. Zaffaroni, M. Costa, and C. G. Riva, "The impact of rain on short E -band radio links for 5G mobile systems: Experimental results and prediction models," *IEEE Transactions on Antennas and Propagation*, vol. 68, no. 4, pp. 3124~3134, Apr. 2020. doi: 10.1109/tap.2019.2957116
10. T. S. Rappaport, R. W. Heath Jr, R. C. Daniels, and J. N. Murdock, *Millimeter wave wireless communications*. Pearson Education, 2015.
11. T. S. Rappaport, S. Sun, R. Mayzus, H. Zhao, Y. Azar, K. Wang, G. N. Wong, J. K. Schulz, M. Samimi, and F. Gutierrez, "Millimeter wave mobile communications for 5G cellular: It will work!" *IEEE Access*, vol. 1, pp. 335~349, 2013. doi: 10.1109/access.2013.2260813
12. L. da Silva Mello and M. S. Pontes, "Unified method for the prediction of rain attenuation in satellite and terrestrial links," *Journal of Microwaves, Optoelectronics and Electromagnetic Applications*, vol. 11, no. 1, pp. 01~14, Jun. 2012. doi: 10.1590/s2179-10742012000100001
13. L. Luini and C. Capsoni, "The SC EXCELL model for prediction of rain attenuation on terrestrial radio links," *Electronics letters*, vol. 49, no. 4, pp. 307~308, 2013. doi: 10.1049/el.2012.3835
14. S.-H. Lin, "A method for calculating rain attenuation distributions on microwave paths," *Bell System Technical Journal*, vol. 54, no. 6, pp. 1051~1086, 1975. doi: 10.1002/j.1538-7305.1975.tb02882.x
15. F. Moupfouma, "Improvement of a rain attenuation prediction method for terrestrial microwave links," *IEEE Transactions on Antennas and Propagation*, vol. 32, no. 12, pp. 1368~1372, 1984. doi: 10.1109/tap.1984.1143248
16. M. Cheffena, "Measurement analysis of amplitude scintillation for terrestrial line-of-sight links at 42 GHz," *IEEE Transactions on Antennas and Propagation*, vol. 58, no. 6, pp. 2021~2028, Jun. 2010. doi: 10.1109/tap.2010.2046869
17. I. Shayea, T. A. Rahman, M. H. Azmi, and A. Arsad, "Rain attenuation of millimetre wave above 10 GHz for terrestrial links in tropical

regions," *Transactions on Emerging Telecommunications Technologies*, vol. 29, no. 8, p. e3450, Jul. 2018. doi: 10.1002/ett.3450

18. V. Ramachandran and V. Kumar, "Modified rain attenuation model for tropical regions for ku-band signals," *International Journal of Satellite Communications and Networking*, vol. 25, no. 1, pp. 53~67, 2006. doi: 10.1002/sat.846
19. ITU-R Recommendations, "Prediction methods required for the design of terrestrial line-of-sight systems, document itu-r p. 530-17," *International Telecommunication Union Radiocommunication Recommendations*, 2017. [Online]. Available: https://www.itu.int/dms_pubrec/itu-r/rec/p/R-REC-P.530-17-201712-S!!PDF-E.pdf (accessed on 14 Jan. 2022)
20. P. Thiennviboon and S. Wisutimateekorn, "Rain attenuation prediction modeling for earth-space links using artificial neural networks," in *2019 16th International Conference on Electrical Engineering/Electronics, Computer, Telecommunications and Information Technology*. Pattaya, Chonburi, Thailand: IEEE, 10~13 Jul. 2019. doi: 10.1109/ECTI-CON47248.2019.8955194
21. C.-S. Lu, Z.-W. Zhao, Z.-S. Wu, L.-K. Lin, P. Thiennviboon, X. Zhang, and Z.-F. Lv, "A new rain attenuation prediction model for the earth-space links," *IEEE Transactions on Antennas and Propagation*, vol. 66, no. 10, Oct. 2018. doi: 10.1109/tap.2018.2854181
22. J. X. Yeo, Y. H. Lee, and J. T. Ong, "Rain attenuation prediction model for satellite communications in tropical regions," *IEEE Transactions on Antennas and Propagation*, vol. 62, no. 11, pp. 5775~5781, Nov. 2014. doi: 10.1109/tap.2014.2356208
23. ITU-R Recommendations, "Rec. ITU-R P. 530-16, propagation data and prediction methods required for the design of terrestrial line-of-sight systems," 2015. [Online]. Available: https://www.itu.int/dms_pubrec/itu-r/rec/p/R-REC-P.530-16-201507-S!!PDF-E.pdf (accessed on 14 Jan. 2022)
24. S. Theodoridis, *Machine learning: a Bayesian and optimization perspective*. Academic press, 2015. ISBN 978-0128015223
25. M. A. Samad and D.-Y. Choi, "Learning-assisted rain attenuation prediction models," *Applied Sciences*, vol. 10, no. 17, p. 6017, Aug. 2020. doi: 10.3390/app10176017

26. C. Han, Y. Bi, S. Duan, and G. Lu, "Rain rate retrieval test from 25-GHz, 28-GHz, and 38-GHz millimeter-wave link measurement in beijing," *IEEE Journal of Selected Topics in Applied Earth Observations and Remote Sensing*, vol. 12, no. 8, pp. 2835~2847, 2019. doi: 10.1109/jstars.2019.2918507
27. D. Wolfensberger, M. Gabella, A. Berne, and U. Germann, "Potential use of specific differential propagation phase delay for the retrieval of rain rates in strong convection over Switzerland," in *UrbanRain18: 11th International Workshop on Precipitation in Urban Areas*. Pontresina, Switzerland: ETH Zurich, Institute of Environmental Engineering, 5~7 Dec. 2019. doi: 10.3929/ethz-b-000347608
28. J. Ostrometzky and H. Messer, "Accumulated rainfall estimation using maximum attenuation of microwave radio signal," in *2014 IEEE 8th Sensor Array and Multichannel Signal Processing Workshop*. A Coruna, Spain: IEEE, 22-25 Jun. 2014. doi: 10.1109/sam.2014.6882373
29. I. Shayea, T. A. Rahman, M. H. Azmi, and M. R. Islam, "Real measurement study for rain rate and rain attenuation conducted over 26 GHz microwave 5G link system in Malaysia," *IEEE Access*, vol. 6, pp. 19 044~19 064, 2018. doi: 10.1109/ACCESS.2018.2810855
30. K. Ulaganathen, T. B. A. Rahman, A. Y. Abdulrahman, and S. K. B. A. Rahim, "Comparative studies of the rain attenuation predictions for tropical regions," *Progress In Electromagnetics Research*, vol. 18, pp. 17~30, 2011. doi: 10.2528/pierm11012602
31. M. Singh and J. E. Allnutt, "Rain attenuation predictions at Ku-band in south east asia countries," *Progress In Electromagnetics Research*, vol. 76, pp. 65~74, 2007. doi: 10.1049/el:20072677
32. S. Lin, "11-GHz radio: nationwide long-term rain rate statistics and empirical calculation of 11-GHz microwave rain attenuation," *Bell System Technical Journal*, vol. 56, no. 9, pp. 1581~1604, 1977. doi: 10.1002/j.1538-7305.1977.tb00582.x
33. L. D. S. Mello, M. Pontes, R. De Souza, and N. P. Garcia, "Prediction of rain attenuation in terrestrial links using full rainfall rate distribution," *Electronics Letters*, vol. 43, no. 25, pp. 1442~1443, 2007. doi: 10.1049/el:20072410
34. A. M. Al-Saman, M. Cheffena, M. Mohamed, M. H. Azmi, and Y. Ai, "Statistical analysis of rain at millimeter waves in tropical

area," *IEEE Access*, vol. 8, pp. 51 044~51 061, 2020. doi: 10.1109/access.2020.2979683

35. S. Shrestha and D.-Y. Choi, "Rain attenuation statistics over millimeter wave bands in South Korea," *Journal of Atmospheric and Solar-Terrestrial Physics*, vol. 152, pp. 1~10, 2017. doi: 10.1016/j.jastp.2016.11.004
36. A. A. H. Budalal, M. R. Islam, K. Abdullah, and T. A. Rahman, "Modification of distance factor in rain attenuation prediction for short-range millimeter-wave links," *IEEE Antennas and Wireless Propagation Letters*, vol. 19, no. 6, pp. 1027~1031, Jun. 2020. doi: 10.1109/lawp.2020.2987462
37. R. Olsen, D. V. Rogers, and D. Hodge, "The aR^b relation in the calculation of rain attenuation," *IEEE Transactions on antennas and propagation*, vol. 26, no. 2, pp. 318~329, 1978. doi: 10.1109/tap.1978.1141845
38. R. K. Crane, "Prediction of the effects of rain on satellite communication systems," *Proceedings of the IEEE*, vol. 65, no. 3, pp. 456~474, 1977. doi: 10.1109/PROC.1977.10498
39. ITU-R Recommendations, "P.838 : Specific attenuation model for rain for use in prediction methods," 2005. [Online]. Available: https://www.itu.int/dms_pubrec/itu-r/rec/p/R-REC-P.838-3-200503-I!!PDF-E.pdf (accessed on 14 Jan. 2022)
40. W. Chujo, T. Manabe, S.-i. Yamamoto, and K. Suzuki, "Dual frequency use technique for 40-GHz satellite communication during rainfall attenuation," in *2015 International Symposium on Antennas and Propagation (ISAP)*. Hobart, TAS, Australia: IEEE, 9~12 Nov. 2015.
41. O. Brisseau, C. Mallet, L. Barthes, and T. Marsault, "Frequency scaling of rain attenuation based on microphysical characteristics for SatCom links," *IEE Proceedings - Microwaves, Antennas and Propagation*, vol. 153, no. 6, p. 523, 2006. doi: 10.1049/ip-map:20050007
42. ITU-R Recommendations, "P.618-13: Propagation data and prediction methods required for the design of earth-space telecommunication systems," ITU-R Recommendations, Report, 2017. [Online]. Available: https://www.itu.int/dms_pubrec/itu-r/rec/p/R-REC-P.618-13-201712-I!!PDF-E.pdf (accessed on 14 Jan. 2022)
43. R. Acharya, "A simple real-time frequency scaling technique for rain attenuation and its performance," *International Journal of Satellite*

Communications and Networking, vol. 38, no. 4, pp. 329~340, 2020. doi: 10.1002/sat.1337

44. S. Bertorelli and A. Paraboni, "Modelling of short-term frequency scaling for rain attenuation using italsat data," *International Journal of Satellite Communications and Networking*, vol. 25, no. 3, pp. 251~262, 2007. doi: 10.1002/sat.867
45. D. Hodge, "Frequency scaling of rain attenuation," *IEEE Transactions on Antennas and Propagation*, vol. 25, no. 3, pp. 446~447, May 1977. doi: 10.1109/tap.1977.1141580
46. F. M. Filho, R. Cole, and A. Sarma, "Millimetre-wave rain induced attenuation: theory and experiment," *IEE Proceedings H-Microwaves, Antennas and Propagation*, vol. 133, no. 4, p. 308, Aug. 1986. doi: 10.1049/ip-h-2.1986.0054
47. J. H. Kim, M.-W. Jung, Y. K. Yoon, and Y. J. Chong, "The measurements of rain attenuation for terrestrial link at millimeter wave," in *2013 International Conference on ICT Convergence (ICTC)*. Jeju, South Korea: IEEE, 14~16 Oct. 2013. doi: 10.1109/ICTC.2013.6675497
48. F. Dintelmann, G. Ortgies, F. Ruecker, and R. Jakoby, "Results from 12-to 30-GHz German propagation experiments carried out with radiometers and the olympus satellite," *Proceedings of the IEEE*, vol. 81, no. 6, pp. 876~884, 1993. doi: 10.1007/978-981-13-5850-0
49. W. L. Stutzman, T. Pratt, A. Safaai-Jazi, P. W. Remaklus, J. Laster, B. Nelson, and H. Ajaz, "Results from the virginia tech propagation experiment using the Olympus satellite 12, 20 and 30 GHz beacons," *IEEE transactions on antennas and propagation*, vol. 43, no. 1, pp. 54~62, 1995. doi: 10.1109/8.366351
50. National Radio Research Agency(RRA), "767, Bitgaram-ro, Najusi, Jeollanam-do 58217, Republic of Korea." Website: http://rra.go.kr/en/index.do (accessed on 14 Jan. 2022)
51. White paper, Cisco public, "Cisco annual internet report (2018–2023)," Cisco, Report, 2020. [Online]. Available: https://www.cisco.com/c/en/us/solutions/collateral/executive-perspectives/annual-internet-report/white-paper-c11-741490.pdf (accessed on 14 Jan. 2022)

52. T. Jiang, J. Zhang, P. Tang, L. Tian, Y. Zheng, J. Dou, H. Asplund, L. Raschkowski, R. D'Errico, and T. Jamsa, "3GPP standardized 5G channel model for IIoT scenarios: A survey," *IEEE Internet of Things Journal*, vol. 8, no. 11, pp. 8799~8815, Jun. 2021. doi: 10.1109/jiot.2020.3048992
53. X. Wang, L. Kong, F. Kong, F. Qiu, M. Xia, S. Arnon, and G. Chen, "Millimeter wave communication: A comprehensive survey," *IEEE Communications Surveys and Tutorials*, vol. 20, no. 3, pp. 1616~1653, 2018. doi: 10.1109/comst.2018.2844322
54. N. Varsier, L.-A. Dufrene, M. Dumay, Q. Lampin, and J. Schwoerer, "A 5G new radio for balanced and mixed IoT use cases: Challenges and key enablers in FR1 band," *IEEE Communications Magazine*, vol. 59, no. 4, pp. 82~87, Apr. 2021. doi: 10.1109/mcom.001.2000660
55. T. S. Rappaport, Y. Xing, G. R. MacCartney, A. F. Molisch, E. Mellios, and J. Zhang, "Overview of millimeter wave communications for fifth-generation (5G) wireless networks—with a focus on propagation models," *IEEE Transactions on Antennas and Propagation*, vol. 65, no. 12, pp. 6213~6230, Dec. 2017. doi: 10.1109/tap.2017.2734243
56. D. Liu, L. Wang, Y. Chen, M. Elkashlan, K.-K. Wong, R. Schober, and L. Hanzo, "User association in 5G networks: A survey and an outlook," *IEEE Communications Surveys and Tutorials*, vol. 18, no. 2, pp. 1018~1044, 2016. doi: 10.1109/comst.2016.2516538
57. T. S. Rappaport, G. R. MacCartney, M. K. Samimi, and S. Sun, "Wideband millimeter-wave propagation measurements and channel models for future wireless communication system design," *IEEE Transactions on Communications*, vol. 63, no. 9, pp. 3029~3056, Sep. 2015. doi: 10.1109/tcomm.2015.2434384
58. Z. Pi and F. Khan, "An introduction to millimeter-wave mobile broadband systems," *IEEE Communications Magazine*, vol. 49, no. 6, pp. 101~107, Jun. 2011. doi: 10.1109/mcom.2011.5783993
59. M. Elkashlan, T. Q. Duong, and H.-H. Chen, "Millimeter-wave communications for 5G: fundamentals: Part I [Guest Editorial]," *IEEE Communications Magazine*, vol. 52, no. 9, pp. 52~54, Sep. 2014. doi: 10.1109/mcom.2014.6894452
60. H. He, Q. Du, H. Song, W. Li, Y. Wang, and P. Ren, "Traffic-aware ACB scheme for massive access in machine-to-machine networks," in

2015 IEEE International Conference on Communications. London, UK: IEEE, 8~12 Jun. 2015. doi: 10.1109/icc.2015.7248390

61. Q. Du, H. Song, Q. Xu, P. Ren, and L. Sun, "Interference-controlled D2D routing aided by knowledge extraction at cellular infrastructure towards ubiquitous CPS," *Personal and Ubiquitous Computing*, vol. 19, no. 7, pp. 1033~1043, Sep. 2015. doi: 10.1007/s00779-015-0872-x
62. Y. Niu, Y. Li, D. Jin, L. Su, and A. V. Vasilakos, "A survey of millimeter wave communications (mmWave) for 5G: opportunities and challenges," *Wireless Networks*, vol. 21, no. 8, pp. 2657~2676, Apr. 2015. doi: 10.1007/s11276-015-0942-z
63. T. Jämsä, P. Kyösti, and K. Kusume, "Deliverable d1. 2 initial channel models based on measurements," *METIS project Deliverable*, 2014.
64. P. B. Papazian, C. Gentile, K. A. Remley, J. Senic, and N. Golmie, "A radio channel sounder for mobile millimeter-wave communications: System implementation and measurement assessment," *IEEE Transactions on Microwave Theory and Techniques*, vol. 64, no. 9, pp. 2924~2932, Sep. 2016. doi: 10.1109/tmtt.2016.2592530
65. I. D. S. Batalha, A. V. R. Lopes, J. P. L. Araujo, B. L. S. Castro, F. J. B. Barros, G. P. D. S. Cavalcante, and E. G. Pelaes, "Indoor corridor and propagation measurements and channel models at 8, 9, 10 and 11 GHz," *IEEE Access*, vol. 7, pp. 55 005~55 021, 2019. doi: 10.1109/access.2019.2911866
66. Y. Okumura, "Field strength and its variability in VHF and UHF land-mobile radio service," *Rev. Electr. Commun. Lab.*, vol. 16, pp. 825~873, 1968.
67. P. E. Mogensen and J. Wigard, "COST Action 231: Digital mobile radio towards future generation system, final report." in *Section 5.2: On antenna and frequency diversity in GSM. Section 5.3: Capacity study of frequency hopping GSM network*. EU publications, 1999.
68. C. Phillips, D. Sicker, and D. Grunwald, "A survey of wireless path loss prediction and coverage mapping methods," *IEEE Communications Surveys and Tutorials*, vol. 15, no. 1, pp. 255~270, 2013. doi: 10.1109/surv.2012.022412.00172

69. K. Haneda, J. Jarvelainen, A. Karttunen, M. Kyro, and J. Putkonen, "A statistical spatio-temporal radio channel model for large indoor environments at 60 and 70 GHz," *IEEE Transactions on Antennas and Propagation*, vol. 63, no. 6, pp. 2694~2704, Jun. 2015. doi: 10.1109/tap.2015.2412147
70. N. O. Oyie and T. J. O. Afullo, "Measurements and analysis of large-scale path loss model at 14 and 22 GHz in indoor corridor," *IEEE Access*, vol. 6, pp. 17 205~17 214, 2018. doi: 10.1109/access.2018.2802038
71. D. P. del Valle, L. Mendo, J. M. Riera, and P. G. del Pino, "Path loss results in an indoor corridor scenario at the 26, 32 and 39 GHz millimeter-wave bands," in *2021 15th European Conference on Antennas and Propagation*. Dusseldorf, Germany: IEEE, 22~26 Mar. 2021. doi: 10.23919/eucap51087.2021.9410907
72. G. R. Maccartney, T. S. Rappaport, S. Sun, and S. Deng, "Indoor office wideband millimeter-wave propagation measurements and channel models at 28 and 73 GHz for ultra-dense 5G wireless networks," *IEEE Access*, vol. 3, pp. 2388~2424, 2015. doi: 10.1109/access.2015.2486778
73. T. S. Rappaport, *Wireless Communications: Principles and Practice*, 2nd ed. Upper Saddle River, NJ, USA: Prentice-Hal, 2002.
74. H. K. Rath, S. Timmadasari, B. Panigrahi, and A. Simha, "Realistic indoor path loss modeling for regular WiFi operations in india," in *2017 Twenty-third National Conference on Communications*. Chennai, India: IEEE, 2~4 Mar. 2017. doi: 10.1109/ncc.2017.8077107
75. S. Geng, J. Kivinen, X. Zhao, and P. Vainikainen, "Millimeter-wave propagation channel characterization for short-range wireless communications," *IEEE Transactions on Vehicular Technology*, vol. 58, no. 1, pp. 3~13, Jan. 2009. doi: 10.1109/tvt.2008.924990
76. A. Ren, Y. Liu, and S. Li, "Simulation and analysis of millimeter-wave propagation characteristics at 60 GHz in corridor environment," in *2020 International Conference on Microwave and Millimeter Wave Technology*. Shanghai, China: IEEE, 20~23 Sep. 2020. doi: 10.1109/icmmt49418.2020.9386660
77. D. Chizhik, J. Du, R. Feick, M. Rodriguez, G. Castro, and R. A. Valenzuela, "Path loss and directional gain measurements at 28 GHz

for non-line-of-sight coverage of indoors with corridors," *IEEE Transactions on Antennas and Propagation*, vol. 68, no. 6, pp. 4820~4830, Jun. 2020. doi: 10.1109/tap.2020.2972609

78. M. Khalily, S. Taheri, S. Payami, M. Ghoraishi, and R. Tafazolli, "Indoor wideband directional millimeter wave channel measurements and analysis at 26 GHz, 32 GHz, and 39 GHz," *Transactions on Emerging Telecommunications Technologies*, vol. 29, no. 10, p. e3311, Apr. 2018. doi: 10.1002/ett.3311
79. M. Aborahama, A. Zakaria, M. H. Ismail, M. El-Bardicy, M. El-Tarhuni, and Y. Hatahet, "Large-scale channel characterization at 28 GHz on a university campus in the united arab emirates," *Telecommunication Systems*, vol. 74, no. 2, pp. 185~199, Jan. 2020. doi: 10.1007/s11235-019-00649-6
80. H. Xu, V. Kukshya, and T. Rappaport, "Spatial and temporal characteristics of 60-GHz indoor channels," *IEEE Journal on Selected Areas in Communications*, vol. 20, no. 3, pp. 620~630, Apr. 2002. doi: 10.1109/49.995521
81. A. M. Al-Samman, T. A. Rahman, M. H. Azmi, M. N. Hindia, I. Khan, and E. Hanafi, "Statistical modelling and characterization of experimental mm-wave indoor channels for future 5G wireless communication networks," *PLOS ONE*, vol. 11, no. 9, p. e0163034, Sep. 2016. doi: 10.1371/journal.pone.0163034
82. K. Haneda, L. Tian, H. Asplund, J. Li, Y. Wang, D. Steer, C. Li, T. Balercia, S. Lee, Y. Kim, A. Ghosh, T. Thomas, T. Nakamurai, Y. Kakishima, T. Imai, H. Papadopoulas, T. S. Rappaport, G. R. MacCartney, M. K. Samimi, S. Sun, O. Koymen, S. Hur, J. Park, J. Zhang, E. Mellios, A. F. Molisch, S. S. Ghassamzadeh, and A. Ghosh, "Indoor 5G 3GPP-like channel models for office and shopping mall environments," in *2016 IEEE International Conference on Communications Workshops*. Kuala Lumpur, Malaysia: IEEE, 23~27 May 2016. doi: 10.1109/iccw.2016.7503868
83. A. M. Al-Samman, T. A. Rahman, T. Al-Hadhrami, A. Daho, M. N. Hindia, M. H. Azmi, K. Dimyati, and M. Alazab, "Comparative study of indoor propagation model below and above 6 GHz for 5G wireless networks," *Electronics*, vol. 8, no. 1, p. 44, Jan. 2019. doi: 10.3390/electronics8010044

84. J. Pascual-García, M.-T. Martinez-Ingles, D. P. Gaillot, J.-M. Molina-García-Pardo, and E. Egea-López, "Experimental wireless channel analysis between 1 and 40 GHz in an indoor NLoS corridor environment," in *2019 International Symposium on Antennas and Propagation (ISAP)*. Xi'an, China: IEEE, 27~30 Oct. 2019.
85. D. Dupleich, R. Müller, S. Skoblikov, C. Schneider, J. Luo, G. Del Galdo, and R. Thomä, "Multi-band indoor propagation characterization by measurements from 6 to 60 GHz," in *2019 13th European Conference on Antennas and Propagation*. Krakow, Poland: IEEE, 31 Mar.~5 Apr. 2019.
86. S. Hafner, D. A. Dupleich, R. Muller, J. Luo, E. Schulz, C. Schneider, R. S. Thoma, X. Lu, and T. Wang, "Characterisation of channel measurements at 70 GHz in indoor femtocells," in *2015 IEEE 81st Vehicular Technology Conference*. Glasgow, UK: IEEE, 11~14 May 2015. doi: 10.1109/vtcspring.2015.7145739
87. V. Nurmela, A. Karttunen, A. Roivainen, L. Raschkowski, V. Hovinen, J. Y. EB, N. Omaki, K. Kusume, A. Hekkala, R. Weiler *et al.*, "Deliverable d1. 4 METIS channel models," in *Proc. Mobile Wireless Commun. Enablers Inf. Soc.(METIS)*, 2015. [Online]. Available: https://metis2020.com/wp-content/uploads/deliverables/METIS_D1.4_v1.0.pdf (accessed on 14 Jan. 2022)
88. W. Fan, I. Carton, J. Ø. Nielsen, K. Olesen, and G. F. Pedersen, "Measured wideband characteristics of indoor channels at centimetric and millimetric bands," *EURASIP Journal on Wireless Communications and Networking*, vol. 2016, no. 1, Feb. 2016. doi: 10.1186/s13638-016-0548-x
89. G. Zhang, K. Saito, W. Fan, X. Cai, P. Hanpinitsak, J.-I. Takada, and G. F. Pedersen, "Experimental characterization of millimeter-wave indoor propagation channels at 28 GHz," *IEEE Access*, vol. 6, pp. 76 516~76 526, 2018. doi: 10.1109/access.2018.2882644
90. ITU Radio Propagation Series, "Rec. P.1238-10. propagation data and prediction methods for the planning of indoor radiocommunication systems and radio local area networks in the frequency range 300 MHz to 450 GHz," ITU-R, Report, 2019. [Online]. Available: https://www.itu.int/dms_pubrec/itu-r/rec/p/R-REC-P.1238-10-201908-I!!PDF-E.pdf (accessed on 14 Jan. 2022)

91. S. Su-hyun, "Is 'real 5G' elusive goal for Korea?" The Korea Herald by Herald Corporation, May 2021. [Online]. Available: http://www.koreaherald.com/view.php?ud=20210530000162 (accessed on 14 Jan. 2022)
92. United States Telecommunications Training Institute, "Spectrum planning at the fcc and emerging technology topics," ITU Telecommunication Development Sector, Tech. Rep., 2020. [Online]. Available: https://www.itu.int/en/ITU-D/Conferences/GSR/2020/Documents/USTTI-ITU_2020-Technolgy-Topics_relelease2_FCC.pdf (accessed on 14 Jan. 2022)
93. Z. Hu, W. Ji, H. Zhao, X. Zhai, A. Saleem, and G. Zheng, "Channel measurement for multiple frequency bands in subway tunnel scenario," *International Journal of Antennas and Propagation*, vol. 2021, pp. 1~13, Jun. 2021. doi: 10.1155/2021/9991758
94. A. Hrovat, G. Kandus, and T. Javornik, "A survey of radio propagation modeling for tunnels," *IEEE Communications Surveys and Tutorials*, vol. 16, no. 2, pp. 658~669, 2014. doi: 10.1109/surv.2013.091213.00175
95. A. Seretis, X. Zhang, K. Zeng, and C. D. Sarris, "Artificial neural network models for radiowave propagation in tunnels," *IET Microwaves, Antennas and Propagation*, vol. 14, no. 11, pp. 1198~1208, Jul. 2020. doi: 10.1049/iet-map.2019.0988
96. J. Li, Y. Zhao, J. Zhang, R. Jiang, C. Tao, and Z. Tan, "Radio channel measurements and analysis at 2.4/5GHz in subway tunnels," *China Communications*, vol. 12, no. 1, pp. 36~45, Jan. 2015. doi: 10.1109/cc.2015.7084382
97. X. Zhang and C. D. Sarris, "Statistical modeling of electromagnetic wave propagation in tunnels with rough walls using the vector parabolic equation method," *IEEE Transactions on Antennas and Propagation*, vol. 67, no. 4, pp. 2645~2654, Apr. 2019. doi: 10.1109/tap.2019.2894285
98. L. Rapaport, G. A. Pinhasi, and Y. Pinhasi, "Millimeter wave propagation in long corridors and tunnels—theoretical model and experimental verification," *Electronics*, vol. 9, no. 5, p. 707, Apr. 2020. doi: 10.3390/electronics9050707
99. J. Boksiner, C. Chrysanthos, J. Lee, M. Billah, T. Bocskor, D. Barton, and J. Breakall, "Modeling of radiowave propagation in tunnels," in

MILCOM 2012 - 2012 IEEE Military Communications Conference. Orlando, FL, USA: IEEE, 29 Oct.~1 Nov. 2012. doi: 10.1109/milcom.2012.6415864

100. M. Liénard and P. Degauque, "Wideband analysis of propagation along radiating cables in tunnels," *Radio Science*, vol. 34, no. 1, pp. 113~122, Jan. 1999. doi: 10.1029/1998rs900007
101. X. Zhang, N. Sood, and C. D. Sarris, "Fast radio-wave propagation modeling in tunnels with a hybrid vector parabolic equation/waveguide mode theory method," *IEEE Transactions on Antennas and Propagation*, vol. 66, no. 12, pp. 6540~6551, Dec. 2018. doi: 10.1109/tap.2018.2864344
102. S. Mahmoud, "Wireless transmission in tunnels with non-circular cross section," *IEEE Transactions on Antennas and Propagation*, vol. 58, no. 2, pp. 613~616, Feb. 2010. doi: 10.1109/tap.2009.2037704
103. C. Zhou, "Ray tracing and modal methods for modeling radio propagation in tunnels with rough walls," *IEEE Transactions on Antennas and Propagation*, vol. 65, no. 5, pp. 2624~2634, May 2017. doi: 10.1109/tap.2017.2677398
104. M. M. Rana and A. S. Mohan, "Segmented-locally-one-dimensional-FDTD method for EM propagation inside large complex tunnel environments," *IEEE Transactions on Magnetics*, vol. 48, no. 2, pp. 223~226, Feb. 2012. doi: 10.1109/tmag.2011.2177075
105. M. Levy, *Parabolic Equation Methods for Electromagnetic Wave Propagation*. IET, Jan. 2000.
106. R. Martelly and R. Janaswamy, "An ADI-PE approach for modeling radio transmission loss in tunnels," *IEEE Transactions on Antennas and Propagation*, vol. 57, no. 6, pp. 1759~1770, Jun. 2009. doi: 10.1109/tap.2009.2019891
107. A. Popov and N. Y. Zhu, "Modeling radio wave propagation in tunnels with a vectorial parabolic equation," *IEEE Transactions on Antennas and Propagation*, vol. 48, no. 9, pp. 1403~1412, 2000. doi: 10.1109/8.898773
108. Y. Hwang, Y. Zhang, and R. Kouyoumjian, "Ray-optical prediction of radio-wave propagation characteristics in tunnel environments. 1. theory," *IEEE Transactions on Antennas and Propagation*, vol. 46, no. 9, pp. 1328~1336, 1998. doi: 10.1109/8.719976

109. Y. Zhang and Y. Hwang, "Theory of the radio-wave propagation in railway tunnels," *IEEE Transactions on Vehicular Technology*, vol. 47, no. 3, pp. 1027~1036, 1998. doi: 10.1109/25.704857

110. C. Zhou, R. Jacksha, and M. Reyes, "Measurement and modeling of radio propagation from a primary tunnel to cross junctions," in *2016 IEEE Radio and Wireless Symposium*. Austin, TX, USA: IEEE, 24~27 Jan. 2016. doi: 10.1109/rws.2016.7444368

111. H. Qiu, J. M. Garcia-Loygorri, K. Guan, D. He, Z. Xu, B. Ai, and M. Berbineau, "Emulation of radio technologies for railways: A tapped-delay-line channel model for tunnels," *IEEE Access*, vol. 9, pp. 1512~1523, 2021. doi: 10.1109/access.2020.3046852

112. F. Hossain, T. Geok, T. Rahman, M. Hindia, K. Dimyati, S. Ahmed, C. Tso, and N. A. Rahman, "An efficient 3-d ray tracing method: Prediction of indoor radio propagation at 28 GHz in 5G network," *Electronics*, vol. 8, no. 3, p. 286, Mar. 2019. doi: 10.3390/electronics8030286

113. S.-H. Chen and S.-K. Jeng, "SBR image approach for radio wave propagation in tunnels with and without traffic," *IEEE Transactions on Vehicular Technology*, vol. 45, no. 3, pp. 570~578, 1996. doi: 10.1109/25.533772

114. C.-H. Teh, B.-K. Chung, and E.-H. Lim, "An accurate and efficient 3-d shooting-and- bouncing-polygon ray tracer for radio propagation modeling," *IEEE Transactions on Antennas and Propagation*, vol. 66, no. 12, pp. 7244~7254, Dec. 2018. doi: 10.1109/tap.2018.2874519

115. S. de Li, Y. jian Liu, L. ke Lin, Z. Sheng, X. chen Sun, Z. peng Chen, and X. jun Zhang, "Channel measurements and modeling at 6 GHz in the tunnel environments for 5G wireless systems," *International Journal of Antennas and Propagation*, vol. 2017, pp. 1~15, 2017. doi: 10.1155/2017/1513038

116. Y. Shen, Y. Shao, L. Xi, H. Zhang, and J. Zhang, "Millimeter-wave propagation measurement and modeling in indoor corridor and stairwell at 26 and 38 GHz," *IEEE Access*, vol. 9, pp. 87 792~87 805, 2021. doi: 10.1109/access.2021.3081822

117. S. Shrestha and D.-Y. Choi, "Rain attenuation study over an 18 GHz terrestrial microwave link in South Korea," *International Jour-*

nal of Antennas and Propagation, vol. 2019, pp. 1~16, Mar. 2019. doi: 10.1155/2019/1712791

118. S. Shrestha and D.-Y. Choi, "Characterization of rain specific attenuation and frequency scaling method for satellite communication in South Korea," *International Journal of Antennas and Propagation*, vol. 2017, pp. 1~16, 2017. doi: 10.1155/2017/8694748
119. Product brochure: Technical overview, "Selecting a signal generator," Keysight Technologies, Inc., Tech. Rep., 2021. [Online]. Available: https://www.keysight.com/kr/ko/assets/7018-03356/technical-overviews/5990-9956.pdf (accessed on 14 Jan. 2022)
120. Product Fact Sheet, "M9393A PXIe performance vector signal analyzer," Keysight Technologies, Inc., Tech. Rep., 2021. [Online]. Available: https://www.keysight.com/kr/ko/assets/7018-04297/product-fact-sheets/5991-4035.pdf (accessed on 14 Jan. 2022)
121. "Chosun university," 2019. [Online]. Available: https://www3.chosun.ac.kr/bbs/museum/309/198803/artclView.do (accessed on 14 Jan. 2022)
122. A. Gharanjik, K. V. Mishra, B. S. MR, and B. Ottersten, "Learning-based rainfall estimation via communication satellite links," in *2018 IEEE Statistical Signal Processing Workshop*. Freiburg, Germany: IEEE, 10~13 Jun. 2018. doi: 10.1109/SSP.2018.8450726
123. J. Heaton, *Introduction to neural networks with Java*. Heaton Research, Inc., 2008. [Online]. Available: https://www.amazon.com/Introduction-Neural-Networks-Java-2nd/dp/1604390085 (accessed on 14 Jan. 2022)
124. C. Wu, M. J. Gales, A. Ragni, P. Karanasou, and K. C. Sim, "Improving interpretability and regularization in deep learning," *IEEE/ACM Transactions on Audio, Speech, and Language Processing*, vol. 26, no. 2, pp. 256~265, 2017. doi: 10.1109/taslp.2017.2774919
125. K. Pu, X. Liu, M. Xian, and T. Gao, "Machine learning classification of rainfall types based on the differential attenuation of multiple frequency microwave links," *IEEE Transactions on Geoscience and Remote Sensing*, 2020. doi: 10.1109/TGRS.2020.2977393
126. A. Ghatak, *Deep Learning with R*. Springer, 2019. ISBN 10.1007/978-981-13-5850-0

127. O. Irsoy and E. Alpaydın, "Unsupervised feature extraction with autoencoder trees," *Neurocomputing*, vol. 258, pp. 63~73, 2017. doi: 10.1016/j.neucom.2017.02.075
128. H. Musafer, A. Abuzneid, M. Faezipour, and A. Mahmood, "An enhanced design of sparse autoencoder for latent features extraction based on trigonometric simplexes for network intrusion detection systems," *Electronics*, vol. 9, no. 2, p. 259, Feb. 2020. doi: 10.3390/electronics9020259
129. K. Abhishek, A. Kumar, R. Ranjan, and S. Kumar, "A rainfall prediction model using artificial neural network," in *2012 IEEE Control and System Graduate Research Colloquium*. Shah Alam, Selangor, Malaysia: IEEE, 16~17 Jul. 2012. doi: 10.1109/ICSGRC.2012.6287140
130. G. R. MacCartney, J. Zhang, S. Nie, and T. S. Rappaport, "Path loss models for 5G millimeter wave propagation channels in urban microcells," in *2013 IEEE Global Communications Conference*. Atlanta, GA: IEEE, 9~13 Dec. 2013. doi: 10.1109/glocom.2013.6831690
131. Winner, II, "WINNER II channel models," *IST-4-027756 WINNER II, D. 1. 1. 2 V1. 2*, 2007.
132. J. Meredith, "Spatial channel model for multiple input multiple output (MIMO) simulations," *Tech-invite, Tech Rep. TR*, vol. 25, 2012.
133. M. K. Samimi, T. S. Rappaport, and G. R. MacCartney, "Probabilistic omnidirectional path loss models for millimeter-wave outdoor communications," *IEEE Wireless Communications Letters*, vol. 4, no. 4, pp. 357~360, Aug. 2015. doi: 10.1109/lwc.2015.2417559
134. A. I. Sulyman, A. T. Nassar, M. K. Samimi, G. R. Maccartney, T. S. Rappaport, and A. Alsanie, "Radio propagation path loss models for 5G cellular networks in the 28 GHz and 38 GHz millimeter-wave bands," *IEEE Communications Magazine*, vol. 52, no. 9, pp. 78~86, Sep. 2014. doi: 10.1109/mcom.2014.6894456
135. S. Piersanti, L. A. Annoni, and D. Cassioli, "Millimeter waves channel measurements and path loss models," in *2012 IEEE International Conference on Communications*. Ottawa, ON, Canada: IEEE, 10~15 Jun. 2012. doi: 10.1109/icc.2012.6363950
136. S. Sun, T. A. Thomas, T. S. Rappaport, H. Nguyen, I. Z. Kovacs, and I. Rodriguez, "Path loss, shadow fading, and line-of-sight probability models for 5G urban macro-cellular scenarios," in *2015 IEEE*

Globecom Workshops. San Diego, CA, USA: IEEE, 6~10 Dec. 2015. doi: 10.1109/glocomw.2015.7414036

137. ITU-R Recommendations, "P.837 : Characteristics of precipitation for propagation modelling," 2017. [Online]. Available: https://www.itu.int/dms_pubrec/itu-r/rec/p/R-REC-P.837-7-201706-I!!PDF-E.pdf (accessed on 14 Jan. 2022)
138. F. D. Diba, T. J. Afullo, and A. A. Alonge, "Rainfall rate and attenuation performance analysis at microwave and millimeter bands for the design of terrestrial line-of-sight radio links in ethiopia," *SAIEE Africa Research Journal*, vol. 107, no. 3, pp. 177~186, Sep. 2016. doi: 10.23919/saiee.2016.8532241
139. F. Norouzian, E. Marchetti, M. Gashinova, E. Hoare, C. Constantinou, P. Gardner, and M. Cherniakov, "Rain attenuation at millimeter wave and low-thz frequencies," *IEEE Transactions on Antennas and Propagation*, vol. 68, no. 1, pp. 421~431, 2019. doi: 10.1109/tap.2019.2938735
140. A. V. R. Lopes, I. S. Batalha, and C. R. Gomes, "Large-scale analysis and modeling for indoor propagation at 10 GHz," *Journal of Microwaves, Optoelectronics and Electromagnetic Applications*, vol. 19, no. 2, p. 276~293, Jun. 2020. doi: 10.1590/2179-10742020v19i2858

List of Publications: Journal Articles

1. **M. A. Samad**, and D.-Y. Choi, "Learning-assisted rain attenuation prediction models," in *Applied Sciences*, vol. 10, no. 17, p. 6017, 2020. doi:10.3390/app10176017. (**IF=2.679**)
2. **M. A. Samad**, F. D. Diba, and D.-Y. Choi, "A survey of rain attenuation prediction models for terrestrial links—current research challenges and state-of-the-art," in *Sensors*, vol. 21, no. 4, p. 1207, 2021. doi: 10.3390/s21041207. (**IF=3.576**)
3. **M. A. Samad**, F. D. Diba, and D.-Y. Choi, "A survey of rain fade models for earth–space telecommunication links—taxonomy, methods, and comparative study," in *Remote Sensing*, vol. 13, no. 10, p. 1965, 2021. doi: 10.3390/rs13101965. (**IF=4.848**)
4. **M. A. Samad**, F. D. Diba, and D.-Y. Choi, "Rain attenuation scaling in South Korea: Experimental results and artificial neural network," in *Electronics*, vol. 10, no. 16, p. 2030, 2021. doi: 10.3390/electronics10162030. (**IF=2.397**)
5. **M. A. Samad**, and D.-Y. Choi, "Scaling of Rain Attenuation Models: A Survey," in *Applied Sciences*, vol. 11, no. 18, p. 8360, 2021. doi: 10.3390/app11188360. (**IF=2.679**)
6. **M. A. Samad**, F. D. Diba, Y. J. Kim, and D.-Y. Choi, "Results of Large-Scale Propagation Models in Campus Corridor at 3.7 and 28 GHz," in *Sensors*, vol. 21, no. 22, p. 7747, 2021. doi: 10.3390/s21227747. (**IF=3.367**)
7. **M. A. Samad**, and D.-Y. Choi, "Analysis and Modeling of Propagation in Tunnel at 3.7 and 28 GHz," in *CMC-Computers, Materials & Continua*, 71(2), pp. 3127–3143, 2022. doi: 10.32604/cmc.2022.023086. (**IF=3.772**)

8. F. D. Diba, **M. A. Samad**, and D.-Y. Choi, "Centimeter and Millimeter-Wave Propagation Characteristics for Indoor Corridors at 3.7 and 28 GHz: Results from Measurements and Models," in *IEEE Access*, vol. 9, pp. 158726-158737, 2021. doi: 10.1109/ACCESS.2021.3130293. (**IF=3.367**)
9. F. D. Diba, **M. A. Samad**, and D.-Y. Choi, "The effects of rain on terrestrial links at K, Ka and E-bands in south korea: Based on supervised learning," in *IEEE Access*, vol. 9, pp. 9345–9355, 2021. doi: 10.1109/access.2021.3049825. (**IF=3.367**)
10. F. D. Diba, **M. A. Samad**, J. Ghimire, and D.-Y. Choi, "Wireless telecommunication links for rainfall monitoring: Deep learning approach and experimental results," in *IEEE Access*, vol. 9, pp. 66 769–66 780, 2021. doi: 10.1109/access.2021.3076781. (**IF=3.367**)

List of Publications: Conference Articles

1. M. A. Samad and D.-Y. Choi, "Radiowave propagation in tunnel: Experimental results," in *Proc. of 7th International Conference on Advanced Engineering and ICT-Convergence 2021*, vol. 4, no. 2. Advanced Engineering and ICT-Convergence Proceedings (AEICP), 2021. ISSN 2635-4586 pp. 209–213.
2. M. A. Samad and D.-Y. Choi, "5G vertical services in Korea," in *Proc. of 6th International Conference on Advanced Engineering and ICT-Convergence 2021*, vol. 4, no. 1. Advanced Engineering and ICT-Convergence Proceedings (AEICP), 2021. ISSN 2635-4586 pp. 173–181.